A&A 507, 671–682 (2009)
DOI: 10.1051/0004-6361/200912675

Astronomy & Astrophysics

Star formation activities of galaxies in the large-scale structures at $z = 1.2$⋆

M. Tanaka[1], C. Lidman[2,3], R. G. Bower[4], R. Demarco[5], A. Finoguenov[6,7], T. Kodama[8], F. Nakata[9], and P. Rosati[1]

[1] European Southern Observatory, Karl-Schwarzschild-Str. 2, 85748 Garching bei München, Germany
e-mail: mtanaka@eso.org
[2] European Southern Observatory, Alonso de Cordova 3107, Casilla 19001, Santiago, Chile
[3] Oskar Klein Center, Roslagstullsbacken 21, 106 91 Stockholm, Sweden
[4] Department of Physics, University of Durham, South Road, Durham DH1 3LE, UK
[5] Department of Astronomy, Universidad de Concepción. Casilla 160-C, Concepción, Chile
[6] Max-Planck-Institut für extraterrestrische Physik, Giessenbachstrasse, 85748 Garching bei München, Germany
[7] University of Maryland, Baltimore County, 1000 Hilltop Circle, Baltimore, MD 21250, USA
[8] National Astronomical Observatory of Japan, Mitaka, Tokyo 181-8588, Japan
[9] Subaru Telescope, National Astronomical Observatory of Japan, 650 North A'ohoku Place, Hilo, HI 96720, USA

Received 10 June 2009 / Accepted 7 September 2009

ABSTRACT

Recent wide-field imaging observations of the X-ray luminous cluster RDCS J1252.9-2927 at $z = 1.24$ uncovered several galaxy groups that appear to be embedded in filamentary structure extending from the cluster core. We make a spectroscopic study of the galaxies in these groups using GMOS on Gemini-South and FORS2 on VLT with the aim of determining if these galaxies are physically associated to the cluster. We find that three groups contain galaxies at the cluster redshift and that they are probably bound to the cluster. This is the first confirmation of filamentary structure as traced by galaxy groups at $z > 1$. We then use several spectral features in the FORS2 spectra to determine the star formation histories of group galaxies. We find a population of relatively red star-forming galaxies in the groups that are absent from the cluster core. While similarly red star forming galaxies can also be found in the field, the average strength of the Hδ line is systematically weaker in group galaxies. Interestingly, these groups at $z = 1.2$ are in an environment in which the on-going build-up of red sequence is happening. The unusual line strengths can be explained by star formation that is heavily obscured by dust. We hypothesize that galaxy-galaxy interactions, which is more efficient in the group environment, is the mechanism that drives these dust obscured star formation. The hypothesis can be tested by obtaining spectral observations in the near-IR, high resolution imaging observations and observations in the mid-IR.

Key words. galaxies: evolution – galaxies: clusters: individual: RDCS J1252-29 – cosmology: large-scale structure of Universe

1. Introduction

Over the course of the last 13 billion years, the Universe has evolved from an almost uniform state to the rich diversity of galaxies that we see locally today. In the local Universe, galaxies in low density regions (commonly referred to as field galaxies) are typically blue late-type galaxies. In sharp contrast to the field, galaxies in high density regions, such as the cores of rich galaxy clusters, are dominated by red early-type galaxies. The dichotomy suggests that the evolution of galaxies is strongly dependent on the environment in which these galaxies live and that environment must play an essential role in shaping the Hubble sequence. While a number of processes to explain this environment-dependent galaxy evolution have been identified (major and minor mergers, galaxy harassment and ram pressure stripping, for example) the effectiveness of each of these processes is still a matter of considerable debate. A direct way to unveil the origin of the environmental dependence of galaxy evolution is to look at galaxies at various redshifts and to quantify how galaxies change their properties as functions of environment and time.

Galaxy clusters and the regions surrounding them are natural laboratories for studying galaxy evolution, because of the wide range of environments – from the dense core to the low density field – that they contain. An emerging picture from studies of clusters at $z < 1$ (e.g., Dressler et al. 1997; Poggianti et al. 1999; Kodama et al. 2001; Balogh et al. 2004; Demarco et al. 2005; Cucciati et al. 2006; Cooper et al. 2007; Koyama et al. 2007; Poggianti et al. 2008; see Tanaka et al. 2005, for a more thorough set of references) is that massive red galaxies were already in place in galaxy clusters by $z \sim 1$. This is in contrast to the field, where a number of studies have shown that the stellar mass function of red galaxies has evolved strongly at $z < 1$ (e.g., Bell et al. 2004; Bundy et al. 2006; Faber et al. 2007). Although there are clear signs of galaxy evolution in clusters (e.g., Cucciati et al. 2006; and Cooper et al. 2007, found an increasing fraction of blue galaxies at higher redshifts), the bulk of the stellar mass in clusters at $z < 1$ are contained within these red and apparently dead galaxies. To understand when and how these galaxies formed, we now need to move to higher redshifts. However, the number of galaxy clusters at $z > 1$ is still very few and our understanding of the galaxy population in $z \gtrsim 1$ clusters is limited (e.g., Blakeslee et al. 2003; Rosati et al. 2004; Stanford et al. 2005; Nakata et al. 2005; Stanford et al. 2006; Lidman et al. 2008; Hilton et al. 2009; Mei et al. 2009).

⋆ Full Table 2 is only available in electronic form at http://www.aanda.org

Most high-z cluster studies are based on broadband photometric data. However, broadband photometry alone does not allow us to examine the star formation histories of galaxies in much detail. Galaxy spectra, on the other hand, are rich in absorption/emission features and can be used to provide a more complete picture of stellar populations and star formation histories. Clusters at $z \gtrsim 1$ are expected to be significantly less evolved than clusters at lower redshift, so they are an ideal place to understand the processes that drive galaxy evolution. Unfortunately, examining $z > 1$ clusters with the same level of detail as that done for $z < 1$ clusters is observationally challenging. This is not only due to the faintness of these very distant galaxies, but also because many prominent features of galaxies at $z > 1$ redshift to >8000 Å, where many of the current optical detectors have low sensitivities. Red sensitive detectors on an 8 m telescope, like FORS2 on VLT, has improved the situation, and it is now feasible to study spectral properties of galaxies at $z \gtrsim 1$ in greater detail. In this paper, we present detailed analyses of stellar populations of galaxies around the RDCSJ 1252.9-2927 cluster at $z = 1.24$ (hereafter RDCSJ1252).

The cluster was originally discovered with ROSAT and Rosati et al. (2004) presented a detailed X-ray analyses based on the deeper Chandra and XMM-Newton data. The cluster exhibits a tight cluster red sequence (Blakeslee et al. 2003; Lidman et al. 2004; Mei et al. 2009). Toft et al. (2004) and Strazzullo et al. (2006) derived the K_s band luminosity function of the cluster galaxies and found that the bright end of the cluster luminosity function has not significantly changed, except for dimming due to passive evolution of an old stellar population. An intensive spectroscopic follow-up campaign was carried out by Demarco et al. (2007). Within the redshift interval $1.22 < z < 1.25$, Demarco et al. (2007) spectroscopically confirmed 38 cluster members and found evidence that the cluster is undergoing a major merger. Holden et al. (2005) performed a fundamental plane analysis based on the deep spectroscopy of the four brightest cluster members. Recently, Gobat et al. (2008) presented a sophisticated spectro-photometric analysis of the cluster galaxies and showed that the cluster galaxies assembled the bulk of their stars over a short time scale and 0.5 Gyr earlier than field galaxies at similar redshifts. Also, Rettura et al. (2008) showed that most of the cluster galaxies have not actively formed stars for the last ~1 Gyr based on deep U-band imaging.

As part of an on-going survey of distant galaxy clusters (Kodama et al. 2005), wide-field multi-band imaging of RDCSJ1252 and the surrounding region were used to study the large-scale structure surrounding the cluster. Tanaka et al. (2007b) reported detecting several significant clumps extending far out from the cluster core. To date, the outskirts of high redshift clusters have not been explored in much detail. The red sequence in the cluster core extends down to faint magnitudes, but the red sequence in the surrounding clumps is sharply truncated at $K_s = 22$ (Tanaka et al. 2007b). As reported by Tanaka et al. (2005), the red sequence in groups at lower redshifts extends to fainter magnitudes. This suggests that some of the blue galaxies in these clumps at $z = 1.24$ will evolve into galaxies on the red sequence. In this paper we report on spectroscopic follow-up observations of these clumps with GMOS on Gemini-South and FORS2 on VLT. We will use these observations to discuss physical process(es) driving the build-up of the red sequence.

The paper is structured as follows. FORS2 and GMOS spectroscopy of galaxies embedded within the clumps found by Tanaka et al. (2007b) are presented in Sect. 2, followed by a discussion on the nature of the clumps in Sect. 3. In Sect. 4, a comparison between the spectral properties of these galaxies and those in both the field and the cluster core will be made. The results are discussed in Sect. 5 and the paper is summarized in Sect. 6. Unless otherwise stated, we adopt $H_0 = 70\ \mathrm{km\,s^{-1}\ Mpc^{-1}}$, $\Omega_M = 0.3$, and $\Omega_\Lambda = 0.7$. Magnitudes are on the AB system. Distances are reported in the comoving reference frame.

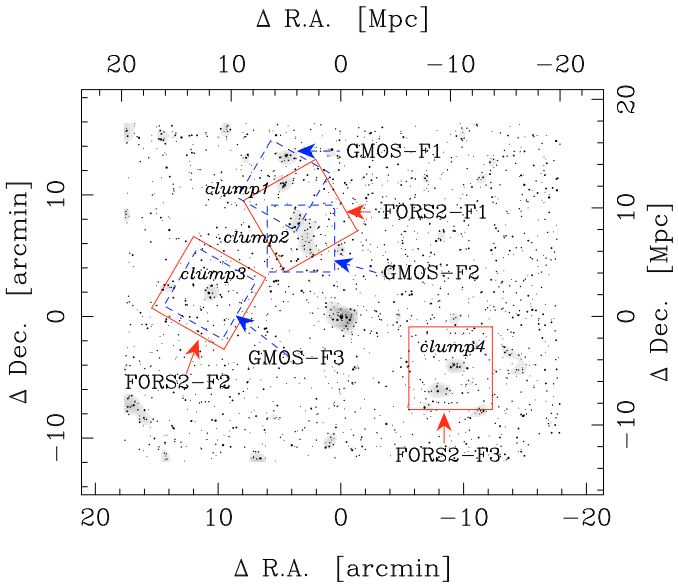

Fig. 1. Distribution of photo-z selected galaxies in RDCSJ1252. The dots show individual galaxies and the shaded regions illustrate the local over-density of such galaxies. The four clumps reported in Tanaka et al. (2007b) are shown with the italic labels. The solid and dashed squares indicate the fields covered by FORS2 and GMOS, respectively. *The top and right-hand* axes are in comoving Mpc.

2. Spectroscopic observations

We used GMOS on Gemini-South (Hook et al. 2004) and FORS2 on VLT UT1 (Appenzeller et al. 1998) to obtain spectroscopic follow-up observations of the structures discovered in Tanaka et al. (2007b). The observations were performed in queue mode, and six fields were observed. The fields cover the most prominent part of the structures, as shown in Fig. 1. The exposure times are listed in Table 1.

2.1. GMOS observations

The GMOS observations were taken between January and March 2007 and were obtained with the R400 grating set to 7800 Å and 7900 Å to fill the detector gaps, and the G5325 order sorting filter. This setting covers the 7000–10 000 Å wavelength range and results in a resolving power of $R \sim 2000$ for a 1″ slit. In order to achieve good sky subtraction in a crowded region, the observations were performed in the nod-and-shuffle mode.

Targets for spectroscopy were selected on the basis of photometric redshifts. Galaxies with $1.0 < z_{\rm phot} < 1.3$ and z-band magnitudes brighter than 23 were given the highest priority. The remaining slits were filled with targets that had colors consistent with star-forming galaxies at $z \sim 1.2$ on the $R - z$ vs. $i - K$ diagram. This supplemental selection was taken because our photometric redshifts may be less accurate for blue galaxies than for red galaxies (Tanaka et al. 2007b), and also because the nod-and-shuffle mode allows one to place slitlets quite densely.

Table 1. Field name and exposure times.

Field ID	Exposure time
GMOS-F1	14×30 min
GMOS-F2	14×30 min
GMOS-F3	6×30 min
FORS2-F1	12×22 min
FORS2-F2	8×22 min
FORS2-F3	2×22 min

The data were reduced with the Gemini data reduction package. The wavelength and flux calibrated 1D spectra were then inspected with custom designed software to compute redshifts and assign confidence flags. Out of 24 galaxies in field F1, 8 secure redshifts (representing a 33% success rate) were obtained. For field F2, 11 redshifts were obtained from 25 galaxies (44% success rate), and for field F3, 14 redshifts were obtained from 31 galaxies (45% success rate). The redshifts were obtained by fitting Gaussians to prominent spectral features such as [OII] and the CaII H and K lines. The redshift errors were estimated through Monte-carlo simulations. We added noise, which was directly estimated from each spectrum, to each data point of the spectrum (i.e., each point fluctuated by its noise). The Gaussian fit was then re-performed. This procedure was repeated 100 000 times and a 68-percentile interval of the redshift distribution is quoted as the error. A confidence flag of 0 indicates a secure redshift. A confidence flag of 1 indicates a possible redshift. Figure 2 presents an example from the GMOS data.

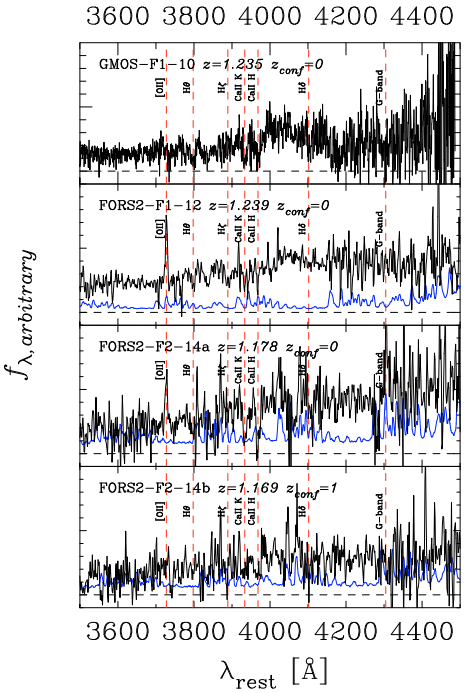

Fig. 2. Sample spectra of galaxies in our catalog from GMOS and FORS2. The dotted line in each panel shows the 1σ error. The error is not plotted in *the top panel* because the GMOS pipeline does not produce an error spectrum. Some of the more prominent spectral features are indicated with the vertical dashed lines. The horizontal dashed lines show the zero flux level.

2.2. FORS2 observations

The FORS2 observations were taken between April and July 2008 and were obtained with the 300*I* grism and the OG590 order sorting filter. This setting covers the 6000–10 000 Å wavelength range and results in a resolving power of $R \sim 500$ for a $1''$ slit. Objects were nodded along the slit in order to facilitate accurate removal of the sky background. Targets for spectroscopy were selected with photometric redshifts. Bright galaxies (z-band magnitude brighter than 23) at $1.0 < z_{\rm phot} < 1.3$ had the highest priority in the slit assignment.

The data reduction was performed with a custom designed reduction package. First, frames were grouped in A-B pairs, where A is one position of the nod and B is the other. These frames were then subtracted from each other, after scaling for differences in the sky background. Cosmic rays were then identified on these sky subtracted frames and were masked out. In order to avoid correlations between pixels, which makes it difficult to estimate flux errors, the 2 dimensional data were not rectified. One dimensional object fluxes and errors were extracted from each A–B pair. The fluctuations in the background are used as a measure of the background noise. All the 1 dimensional spectra in each slitlet were then combined. Wavelength shifts caused by instrument flexures and optical distortions were corrected by tracing the relative positions of the sky lines. The wavelengths were then calibrated using sky lines, and fluxes were calibrated with spectroscopic standard stars. The strong telluric absorption at ~9300 Å was corrected using the spectra of stars that were observed in the same mask.

All spectra were visually inspected. Redshifts and confidence flags were assigned in the same way as that done for the GMOS spectra. Out of 31 galaxies in field F1, 30 secure redshifts (representing 97% of the sample) were obtained. For field F2, 30 redshifts were obtained from 36 galaxies (83% success rate), and for field F3, 13 redshifts were obtained from 31 galaxies (43% success rate). The low success rate in F3 is because only a fraction of the requested total exposure was obtained (see Table 1). The overall success rate of the FORS2 observations is very high compared to the GMOS observations. This is largely due to relative sensitivity of the FORS2 CCDs at ~9000 Å, where the most prominent spectral features of $z \sim 1.2$ galaxies land. The FORS2 spectra have a high enough signal for detailed spectral analyses; the median signal to noise ratio of the spectra with secure redshifts is ~3 per Å at 3900 Å $< \lambda_{\rm rest} <$ 4100 Å. We present spectral properties of galaxies using the FORS2 spectra in Sect. 4.

2.3. Combined spectroscopic catalog

The redshifts from the GMOS and FORS2 observations were compiled into a single spectroscopic catalog. The catalog contains 102 objects with secure redshifts and 18 objects with possible redshifts. The catalog is presented in Table 2. One object has a secure redshift from both FORS2 and GMOS. The difference between the two measurements is $z_{\rm GMOS} - z_{\rm FORS2} = -0.001$. To the GMOS and FORS2 catalog, we add objects published in Demarco et al. (2007) to create a combined catalog. The combined catalog covers a wide range of environments at $z = 1.24$ – from the dense cluster core to the surrounding lower-density field. In the following sections, an analysis of the distribution and properties of these galaxies will be presented. Only objects with secure redshifts are used in this analysis.

Table 2. The GMOS and FORS2 spectroscopic catalog, listing the object name (ID), the coordinates in J2000, the redshift, the confidence flag (0 for a secure redshift and 1 for a possible redshift), and the total magnitudes and their errors.

ID	RA	Dec.	Redshift	Flag	V	$\sigma(V)$	R	$\sigma(R)$	i	$\sigma(i)$	z	$\sigma(z)$	K	$\sigma(K)$
GMOS-F1-4	12 53 16.63	–29 17 11.6	$1.0706^{+0.0001}_{-0.0001}$	0	25.40	0.12	25.46	0.12	25.03	0.12	24.69	0.20	24.63	0.81
GMOS-F1-5	12 53 17.44	–29 17 00.8	$1.0684^{+0.0001}_{-0.0001}$	1	24.51	0.09	24.31	0.08	23.91	0.08	23.39	0.11	22.08	0.20
GMOS-F1-6	12 53 09.02	–29 16 47.6	$1.0976^{+0.0007}_{-0.0010}$	1	26.37	0.47	24.44	0.10	23.54	0.07	22.70	0.07	21.03	0.10
GMOS-F1-9	12 53 16.03	–29 16 17.2	$1.2452^{+0.0003}_{-0.0002}$	1	24.23	0.20	23.57	0.10	22.71	0.07	21.77	0.07	19.87	0.07
GMOS-F1-10	12 53 15.43	–29 16 23.7	$1.2354^{+0.0004}_{-0.0004}$	0	24.56	0.57	22.76	0.11	21.86	0.06	20.96	0.05	19.06	0.05
GMOS-F1-11	12 53 14.92	–29 16 13.4	$1.2368^{+0.0011}_{-0.0013}$	0	25.34	0.30	24.07	0.10	23.09	0.07	22.19	0.06	20.17	0.07
GMOS-F1-12	12 53 15.96	–29 16 29.9	$1.2839^{+0.0008}_{-0.0007}$	1	25.49	0.28	24.08	0.08	23.67	0.09	22.86	0.09	20.98	0.11
GMOS-F1-13	12 53 15.28	–29 16 29.8	$1.0699^{+0.0006}_{-0.0003}$	0	26.49	0.58	23.80	0.06	23.43	0.07	22.49	0.07	20.77	0.09
GMOS-F1-14	12 53 16.22	–29 16 38.4	$1.0698^{+0.0001}_{-0.0001}$	0	24.22	0.10	23.55	0.06	23.01	0.05	22.52	0.07	20.98	0.11
GMOS-F1-21	12 53 16.41	–29 15 44.0	$1.1797^{+0.0004}_{-0.0005}$	1	23.32	0.04	23.14	0.03	23.19	0.05	23.25	0.11	22.29	0.25

Magnitudes are on the AB system. The redshift error does not include wavelength calibration error which is typically 0.2 Å. The magnitude of strongly blended objects is listed with a -1. *The table will appear in its entirety as supplemental material.*

3. Large-scale structures at $z = 1.24$

3.1. Spectroscopic confirmation of the structures

Let us start with the conclusion of this section – two of the four clumps identified in Tanaka et al. (2007b) contain galaxies at the cluster redshift. The clumps are embedded in a filamentary structure that extends northwards from the cluster core. In addition, a new clump is discovered and it lies in a second structure that extends eastwards from the cluster. Refer to Fig. 1 for the location of these clumps. The properties of each clump are summarized in Table 3.

– **Clumps 1 and 2 (Fig. 3)**: these two clumps lie to the north of the RDCSJ1252 and both contain concentrations of galaxies close to the cluster redshift. Clump 1 contains 5 spectroscopically confirmed members. Its redshift is very close to the cluster redshift ($z = 1.237$; Demarco et al. 2007). Here, galaxies with $|z - z_{\rm clump}| < 0.005$ are defined as clump members. This window is wide enough to include most members, while it is small enough to exclude apparent outliers. The same criterion is used for the other clumps. Clump 1 is 12 Mpc away (transverse distance) from the cluster core.
  Clump 2, which lies in between clump 1 and the cluster core, is also confirmed to be real. Interestingly, the redshift distribution of clump 2 is bimodal as indicated in Fig. 3 – one peak at $z = 1.214$ and the other at $z = 1.234$. The line of sight distance between the two peaks is ∼40 Mpc. They are called clump 2a and 2b in Table 3, respectively. Clump 2a has 6 spectroscopically confirmed members, however, the galaxies are not spatially concentrated very strongly. On the other hand, clump 2b shows a clear spatial concentration of galaxies at the cluster redshift.
  Extended X-ray emission from clumps 1 and 2 was reported in Tanaka et al. (2007b). Clump 2b is most likely the counterpart of the detected X-ray emission in that area because clump 2a has a looser spatial distribution. As we will show in the next subsection, clump 2a is dynamically independent from the RDCSJ1252 cluster. The detection of X-ray emission from both clump 1 and clump 2b support the notion that both clumps are bound systems;
– **Clump 3 (Fig. 4)**: this clump is located 10 Mpc eastwards from the cluster core. The spectroscopy shows a strong concentration at $z = 1.175$, which is more than 100 Mpc away from the cluster along the line of sight. We call this system clump 3a. Although it is likely that clump 3a is a physically bound system with its strong redshift and spatial concentrations, this clump is dynamically independent from the cluster at $z = 1.237$. This clump is marginally detected in X-rays at the 2.4σ level (Tanaka et al. 2007b).
  It is interesting to note that there is a second strong redshift peak at the cluster redshift in this area. A clump of galaxies 2 Mpc eastwards of clump 3a is responsible for this peak. This clump is labeled clump 3b and is likely to be a physically bound system given the clear redshift and spatial concentration. Clump 3b indicates that there is a structure extending eastwards from the RDCSJ1252 cluster;
– **Clump 4 (Fig. 5)**: only 44min of integration was obtained in this field, which resulted in relatively few redshifts. Two galaxies at the center of the over-density have $z \sim 1.17$ and it is thus likely that clump 4 is a foreground system. We observe two other galaxies at $z = 1.15$ and another two at $z = 1.19$ in the same field; however, they land outside the clump. Overall, there are too few redshifts to decide if clump 4 is a bound system.

The large-scale structure surrounding RDCSJ1252 is illustrated in Fig. 6. Galaxies from Demarco et al. (2007) are also plotted. At least two structures are detected: a filament extending northwards from the center of the cluster and hosting clumps 1 and 2b and a group lying eastwards of the cluster and hosting clump 3b.

3.2. Dynamical analysis

To quantify the relationship between the clumps and the cluster, we use the Newtonian energy integral formalism (Beers et al. 1982; Hughes et al. 1995; Lubin et al. 1998) to compute the probabilities that the clumps are bound to RDCSJ1252. We introduce the position angle ϕ_d between a clump and the cluster relative to the line-of-sight. The linear distance between them is then given by $d = D_{\rm p}/\sin\phi_d$, where $D_{\rm p}$ is the transverse distance. Similarly, the relative space velocity between them is represented as $v = v_r/\cos\phi_v$, where v_r is the line-of-sight velocity difference and ϕ_v is the angle in velocity space relative to the line-of-sight. The condition that a clump and the cluster are bound is then expressed as

$$v_r^2 - (2GM/D_{\rm p})\sin\phi_d\cos^2\phi_v < 0, \quad (1)$$

where M is the total mass of the system. The probability that a clump is dynamically bound to the cluster is equivalent to

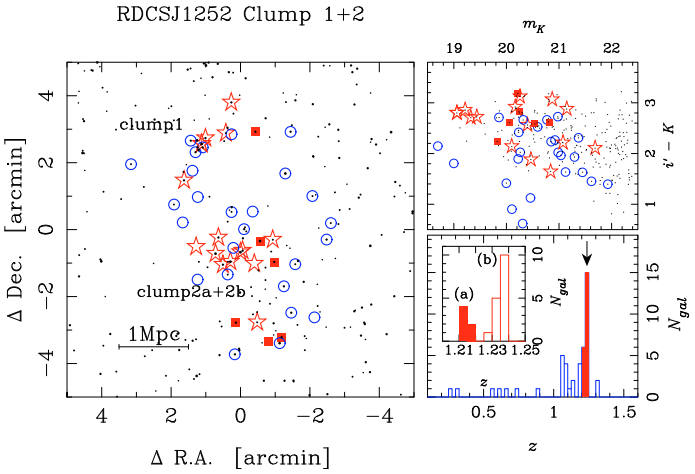

Fig. 3. *Bottom-right panel*: the redshift distribution of galaxies. The inset zooms in at the cluster redshift, which is indicated by the arrow. *Top-right panel*: the color magnitude diagram. The filled squares and open stars show galaxies at $z \sim 1.21$ and $z \sim 1.23$, respectively. The dots are galaxies with $1.0 < z_{\rm phot} < 1.3$. Open circles are spectroscopically confirmed foreground/background galaxies. *Left panel*: the spatial distribution of galaxies. The symbols are the same as those in *the top-right panel*.

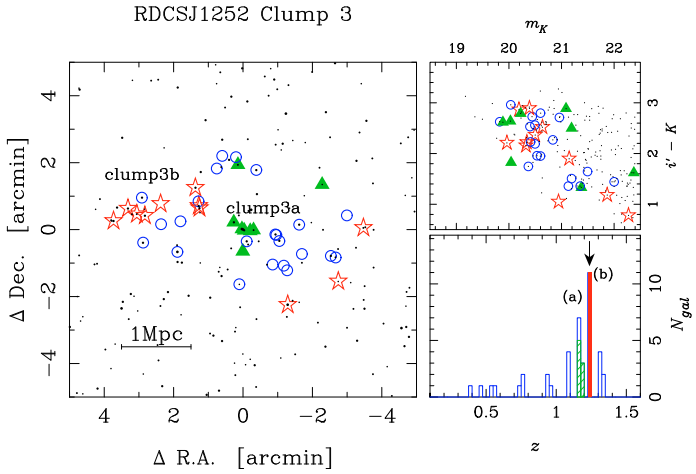

Fig. 4. Same as Fig. 3, but for clumps 3a (hatched histogram and filled triangles) and 3b (filled histogram and open stars).

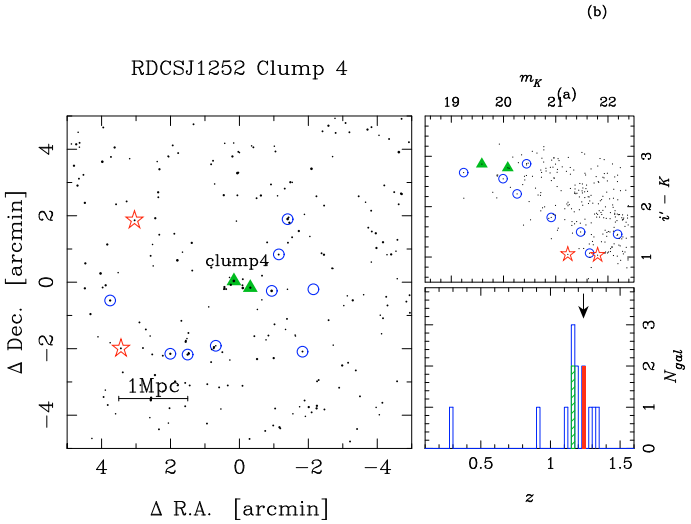

Fig. 5. As for Fig. 3, but for clump 4.

estimating the fraction of the solid angle (ϕ_d and ϕ_v) that satisfies Eq. (1).

Assuming that RDCSJ1252 is virialized, we derive a cluster mass of $M_{200} = 3.7^{+1.0}_{-1.1} \times 10^{14}\ M_\odot$ from the galaxy velocity dispersion. Within the errors, this estimate is consistent with the one derived from X-ray observations ($2.7 \times 10^{14}\ M_\odot$; Rosati et al. 2004). Demarco et al. (2007) reported that the cluster might consist of two merging clusters and that the total mass of the two clusters is $2.7 \times 10^{14}\ M_\odot$, consistent with the X-ray estimate. Cluster masses can be estimated in a number of ways, but each method has its own systematic uncertainties (e.g., masses from velocity dispersions can be affected by substructure). Considering these estimates, we use a mass of $3^{+1}_{-1} \times 10^{14}\ M_\odot$ for deriving the bound probabilities. The probabilities are summarized in Table 3.

– **Clump 1**: Clump 1, with a bound probability of ~90%, is probably bound to RDCSJ1252, although its transverse separation is 12 Mpc;
– **Clump 2**: Clump 2b, with a bound probability of ~50%, may also be bound to the cluster. Therefore, the filamentary structure extending northwards of the cluster core is within the gravitational reach of the cluster. Clump 2a is probably not a bound system in itself given the loose spatial distribution of the galaxies within this clump. Assuming that it has a similar mass and transverse distance as clump 2b (note that small changes to the clump mass and transverse distance have little effects on the bound probability – the mass of the central cluster and line-of-sight velocity difference are the key parameters.), the bound probability is 0, suggesting that the structure hosting clump 2a is unrelated to RDCSJ1252;
– **Clump 3**: Clump 3a is a foreground system at $z = 1.17$ and is not bound to the cluster (0% bound probability). Clump 3b provides evidence for structure extending eastwards of the cluster. It is bound to the cluster with a ~50% probability, a relatively high probability considering it has a transverse separation of 15 Mpc from the cluster. The cluster itself is elongated in the East-West direction (Demarco et al. 2007), thus suggesting that it may have experienced a merger with a group of galaxies that fell along the direction leading to clump 3b;
– **Clump 4**: there are not enough redshifts to estimate the mass of clump 4. Using the mass for clump 3a as an upper limit (note that clump 3a is marginally detected in X-rays whereas clump 4 is not), it is unlikely (bound probability of 0%) that clump 4 is bound to the cluster.

To sum up, some of the spectroscopically confirmed structures are probably bound to RDCSJ1252. There appears to be two filaments leading to the cluster: a very clear one extending towards the north hosting clumps 1 and 2b, and another one extending towards the east hosting clump 3b. The structure containing clump 2a at $z = 1.21$ and extending to the north is probably not associated to the central cluster as suggested from its bound probability. The other two clumps, clump 3a and clump 4, are dynamically independent of the cluster.

This is the first secure confirmation of filamentary structure at $z > 1$ as traced by groups of galaxies. Such groups enable us to examine how environment affects the evolution of galaxies at high redshifts. We take this opportunity and look into the spectral properties of these galaxies in the next section using the high quality FORS2 spectra described in Sect. 2.2.

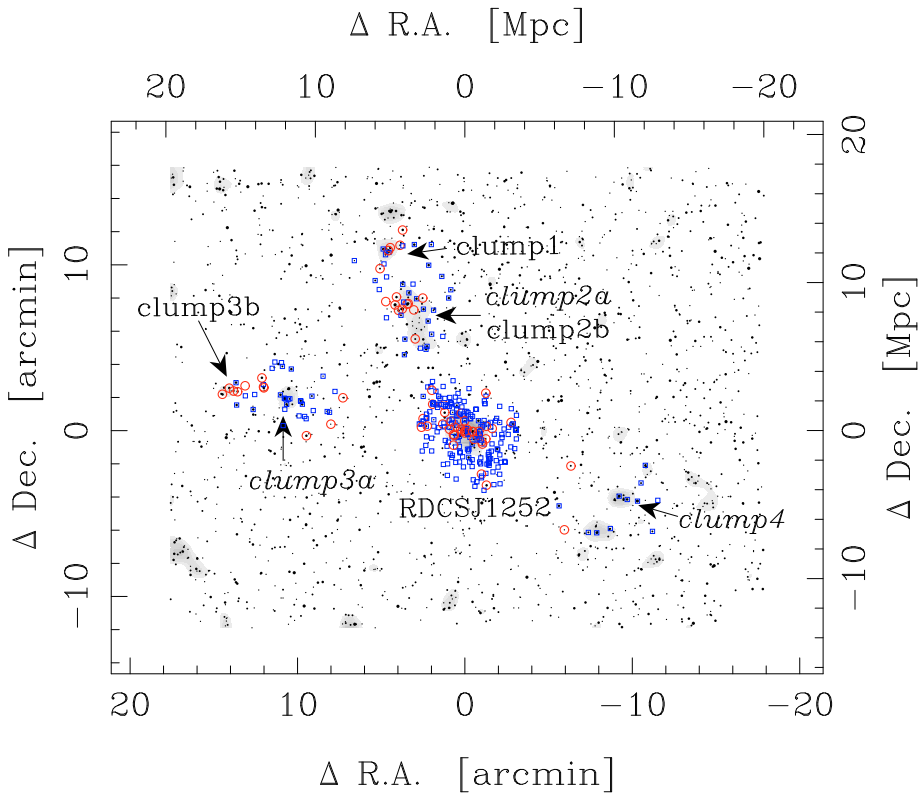

Fig. 6. The large-scale structure surrounding RDCSJ1252. Dots represent photo-z selected galaxies and the shaded regions show the local over-density of these galaxies. The spectroscopically confirmed bound systems are indicated with labels (the italic labels show the foreground systems). Circles are galaxies at $1.22 < z < 1.25$ and squares are those outside of this redshift range. Note that the RDCSJ1252 cluster is at $z = 1.237$ (Demarco et al. 2007).

Table 3. Properties of the clumps.

	$N_{\rm spec.member}$	z	σ [kms^{-1}]	R_{200} [Mpc]	M_{200} [$M_\odot$]	$P_{\rm bound}$
RDCSJ1252 cluster	38	$1.2370^{+0.0009}_{-0.0011}$	754^{+55}_{-89}	$0.93^{+0.07}_{-0.11}$	$3.7^{+0.9}_{-1.1} \times 10^{14}$	–
Clump 1	5	$1.2365^{+0.0002}_{-0.0015}$	44^{+271}_{-5}	$0.05^{+0.33}_{-0.01}$	$7.6^{+270}_{-2.5} \times 10^{11}$	86^{+7}_{-36}
Clump 2a	6	$1.2135^{+0.0010}_{-0.0013}$	287^{+36}_{-159}	$0.36^{+0.04}_{-0.20}$	$2.1^{+0.9}_{-1.9} \times 10^{13}$	0^{+0}_{-0}
Clump 2b	10	$1.2343^{+0.0012}_{-0.0013}$	517^{+97}_{-164}	$0.64^{+0.12}_{-0.20}$	$1.2^{+0.8}_{-0.8} \times 10^{14}$	51^{+28}_{-28}
Clump 3a	8	$1.1748^{+0.0015}_{-0.0019}$	435^{+32}_{-200}	$0.55^{+0.04}_{-0.25}$	$7.3^{+1.7}_{-6.2} \times 10^{13}$	0^{+0}_{-0}
Clump 3b	8	$1.2350^{+0.0005}_{-0.0008}$	235^{+41}_{-94}	$0.29^{+0.05}_{-0.12}$	$1.1^{+0.7}_{-0.9} \times 10^{13}$	47^{+28}_{-27}
Clump 4	2	1.1745	–	–	–	0^{+0}_{-0}

The second column shows the number of spectroscopically confirmed members in each clump. Redshifts (3rd column) and velocity dispersions (4th column) are estimated with the biweight estimator (Beers et al. 1990). The redshift errors are estimated by bootstrapping, taking into account individual redshift errors. The 5th and 6th columns show the Virial radii and masses (Carlberg et al. 1997). The last column shows the probability that each clump is dynamically bound to RDCSJ1252. The galaxies in clump2a are not spatially concentrated, suggesting that this clump probably not a bound system. There are only two members in clump 4 and the redshift is an average redshift of these two galaxies. The properties of RDCSJ1252 are added for reference. See text for details.

4. Spectral analyses

Following the confirmation of the large-scale structure surrounding RDCSJ1252, we now use the FORS2 spectra presented here and published elsewhere (Holden et al. 2005; van der Wel et al. 2005; Demarco et al. 2007) to examine the spectral properties of galaxies as a function of environment. We define three environments – cluster, group, and field. Cluster galaxies are spectroscopically confirmed members within 1 Mpc (physical) of the cluster center (Demarco et al. 2007). The group galaxies are defined as those that are within the clumps confirmed in this paper, except for clump 2a as it is probably not dynamically bound. Clump 3a is a dynamically independent foreground group, but we include it to gain statistics given that it and RDCSJ1252 have similar redshifts ($\Delta z = -0.06$). Note that our results remain unchanged if we exclude it. The other galaxies at $1.15 < z < 1.25$ (e.g., galaxies in the clump2a) are regarded as field galaxies. In the following, we first study the star formation activity in these galaxies by examining [OII] equivalent widths, strengths of the 4000 Å break, and broad-band $i - K_{\rm s}$ colors. We then examine Hδ equivalent widths.

A fraction of the observed [OII] emissions might arise from AGN activity rather than from star formation. To quantify the AGN contamination, we search for point sources in the 0.5–2 keV band data of the XMM observations reported in Tanaka et al. (2007b). Within the area covered by XMM, we have recovered all point sources with L_X exceeding 7×10^{42} erg s^{-1} in the rest frame 0.5–2 keV band assuming a power law of $\Gamma = 1.8$ and the redshift of the cluster, therefore sampling well the typical AGN luminosities. We find that none of the galaxies we discuss below are detected in X-ray, giving AGN fractions of $0^{+0.029}_{-0}$, $0^{+0.035}_{-0}$, $0^{+0.084}_{-0}$, in cluster, group, and field

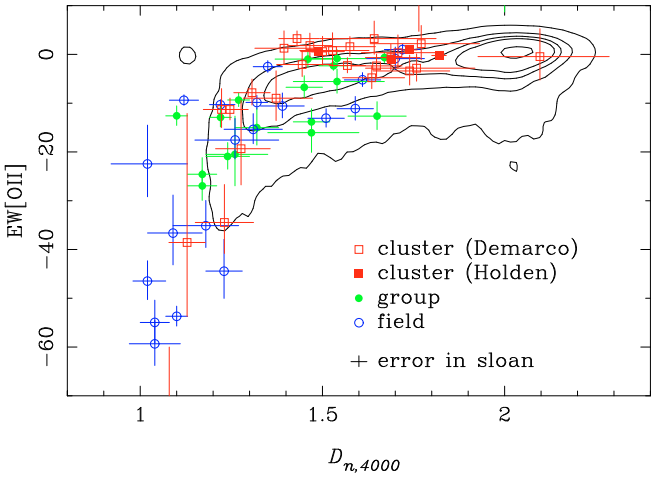

Fig. 7. *EW*[OII] plotted against $D_{n,4000}$ for galaxies in the cluster, the groups and the field. The symbols are defined in the plot. The distribution for galaxies in SDSS is plotted as contours for comparison. The contours enclose 5, 25, 50, 75 and 95 percent of the galaxy population. The typical error in the SDSS data is shown in the plot.

environments, respectively. The errors are Poisson errors. These fractions are fully consistent with those from the COSMOS survey (Silverman et al. 2009), although X-ray flux limits and stellar mass limits are different and comparisons are not straightforward. We regard the observed [OII] emissions arise from star forming regions, not from AGNs. Note that Yan et al. (2006) found that ∼30% of red galaxies at $z = 0$ are LINERs, but such weak AGNs are unlikely to affect our results significantly.

4.1. Star formation activity as a function of environment

The [OII] equivalent width (*EW*[OII]) is plotted against the strength of the 4000 Å break ($D_{n,4000}$) in Fig. 7. The *EW*[OII] is estimated following Fisher et al. (1998). For the 4000 Å break, the definition specified in Balogh et al. (1999) is used. This definition uses narrow wavelength windows to measure the break, which minimizes the effects of the strong telluric absorption feature at ∼9300 Å. Although we remove the absorption from this region (see Sect. 2.2), we avoid this region in the analysis in order to minimize systematic errors. Measurement errors of these spectral indices are estimated via monte-carlo simulations. For the cluster data, we estimate the average noise around the spectral features. For the group and filament data, we have a noise spectrum for each object. The noise is randomly added to each data point of the spectra and we repeated the measurements 100 000 times. A 68-percentile interval is taken as an error.

Local galaxies from Tanaka et al. (2007a) are plotted for comparison. They are from the Sloan Digital Sky Survey (SDSS, York et al. 2000; Strauss et al. 2002) and have $M_V < M_V^* + 1$ at $0.005 < z < 0.065$. Our spectroscopy reaches a z-band magnitude of ∼23, which roughly corresponds to $m_z^* + 1$ at $z = 1.2$ for red galaxies with $z - Ks \sim 2$ (Toft et al. 2004; Strazzullo et al. 2006). The magnitude cut applied to the SDSS data is relative to M_V^* at $z = 0$. We thus sample the similar luminosity ranges both at $z = 0$ and 1.2 relative to the evolving characteristic magnitudes measured at each redshift. We use the SDSS data only to illustrate the range of spectral indices that $z = 0$ galaxies have.

Most of the spectra in Demarco et al. (2007) were taken before FORS2 was upgraded with the red sensitive MIT/LL detectors, so the flux calibration beyond 9000 Å is not sufficiently precise enough for computing $D_{n,4000}$. In order to use these data, a posteriori corrections to the calculated values of $D_{n,4000}$ were applied using the $i - z$ colors. The corrections applied are typically $\Delta D_{n,4000} \sim 0.1$. The validity of applying this correction was verified using the high-signal to noise spectra in Holden et al. (2005). There, $D_{n,4000,\mathrm{calib}} - D_{n,4000,\mathrm{Holden}} \sim -0.1$. We adopt 0.1 as our systematic error in estimating $D_{n,4000}$ for the spectra from Demarco et al. (2007). The impact on computing *EW*[OII] is negligible as it is measured in a narrow wavelength window.

Galaxies at $z \sim 1.2$, independent of environment, show smaller $D_{n,4000}$ than local galaxies. For example, galaxies at $z = 0$ form a locus of red galaxies at $D_{n,4000} \sim 2$, while red galaxies at $z \sim 1.2$ have $D_{n,4000} \sim 1.6$. This is consistent with passive evolution of red galaxies from $z \sim 1.2$ to $z \sim 0$. Blue galaxies at $z \sim 1.2$ are bluer than local blue galaxies, suggesting more active star formation at $z \sim 1.2$ than $z = 0$ (Blanton 2006). Overall, all types of galaxies at $z \sim 1.2$ are bluer than local galaxies.

At $z \sim 1.2$, there are galaxies in the field and in the groups that have both red colors ($D_{n,4000} \sim 1.6$) and significant [OII] emission (*EW*[OII] < -10Å). The fractions of red star-forming galaxies, defined here as $1.4 < D_{n,4000} < 1.7$ and *EW*[OII] < -10 Å, in groups and in the field are 0.33 ± 0.22 and 0.40 ± 0.33, respectively. Such red star-forming galaxies are not observed in the cluster. In clusters at slightly lower redshifts (e.g., Geach et al. 2006; Marcillac et al. 2007; Koyama et al. 2008) it has been shown that dusty, star-forming galaxies preferentially reside in low to medium density regions. For reference, the fraction of red star forming galaxies in the local Universe (defined here as $1.8 < D_{n,4000} < 2.2$ and *EW*[OII] < -10 Å) is 0.06 ± 0.01.

We further illustrate the characteristics of these red star-forming galaxies with a color-magnitude plot, as shown in Fig. 8. The i and K band photometry is from Suprime-Cam and WFCAM, respectively (Tanaka et al. 2007b). The cluster is dominated by red galaxies without strong [OII] emission. A tight red sequence in groups is also formed by galaxies without [OII], but there are some [OII] emitting galaxies on the red sequence. The field galaxies show a significant fraction of red star-forming galaxies even on the red sequence, although the red sequence is broader than it is for the groups and the cluster. We note that the slightly wider redshift range adopted for the field sample does not strongly contribute to the observed large scatter. At $1.15 < z < 1.25$, the k-correction for the $i - K_s$ color is only ∼0.1 mag for passively evolving galaxies, which is small compared to the observed color spread of the field galaxies ($2.5 < i - K_s < 3.4$ at $K_s \sim 20.4$). We perform a linear fit to the cluster red sequence, shown as the solid lines in Fig. 8, and find that the fractions of [OII] emitters (*EW*[OII] < -10 Å) within $\Delta|i - K| < 0.5$ mag from the red sequence are 0.09 ± 0.10, 0.26 ± 0.14, and 0.27 ± 0.16 in the cluster, group and field environments, respectively. Although the errors are large, there are more star-forming galaxies on the red sequence in group and field environments. We will discuss these galaxies in detail later.

The figure shows that we typically sample red galaxies with $20 < K < 21.5$ and blue galaxies down to $K \sim 22.5$ in all the environments. The cluster galaxies are from Demarco et al. (2007), but their magnitude and color distributions are not strongly different from those of the group and field galaxies. Therefore, the spectral differences we observe are unlikely due to sample biases. Note that there are more massive galaxies in higher density regions, but it is due to the environmental dependence of the

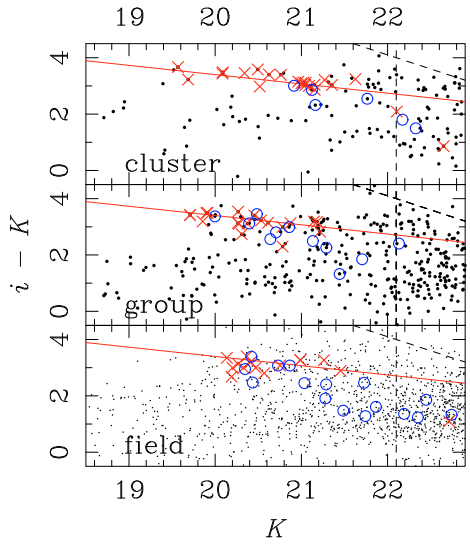

Fig. 8. $i - K$ plotted against K for galaxies in the cluster, group and field environments. The open circles (crosses) represent galaxies with (without) significant [OII] emission (EW[OII] < -10 Å). The points show all objects within 1′ from the center of each clump. The dashed lines show 5σ detection limits. The solid straight lines are fits to the cluster red sequence.

stellar mass function. We discuss the stellar mass dependence of the spectral indices later.

4.2. Detailed star formation history of galaxies

We now take a deeper look into the spectral properties of the galaxies in the groups and field surrounding RDCSJ1252. Among many spectral features that are sensitive to star formation, the Hδ absorption is particularly interesting because it is sensitive to star formation rates about 0.1–1 Gyr prior to the observed epoch. It is noteworthy that Hδ at $z = 1.24$ lands in a region that is free of bright night sky lines. The gap is one of the reddest OH windows in the optical regime, and $z = 1.24$ is probably the highest redshift at which Hδ is still accessible with optical spectrographs. Our FORS2 spectra are good enough to measure Hδ line strengths. Unfortunately, most of the cluster spectra from Demarco et al. (2007) were taken with the original FORS2 CCD, which was not very sensitive beyond 9000 Å. The Hδ absorption is around ~9200 Å in the observed frame and these cluster spectra do not have a sufficient signal there. We instead use the spectra from Holden et al. (2005) with the caveat that they are the brightest cluster members, so they sample a luminosity range that is not available to galaxies in groups and in the field.

We use the definition of Hδ_F described in Worthey & Ottaviani (1997), which uses a narrower spectral window than Hδ_A. The Hδ line at $z = 1.24$ is close to a strong telluric absorption feature, which lands at ~9300 Å, and we prefer the narrow window to minimize effects from this feature, although we do correct all spectra for it. The contribution to Hδ from nebular emission was corrected using the strength of the [OII] emission line. The [OII] flux was first translated into an Hα flux assuming the local relation from Kennicutt (1998), which was then translated into an Hδ flux assuming $A_{H\alpha} = 1$ mag. of extinction and the extinction law from Cardelli et al. (1989). To be specific, we used the relation H$\delta = 0.09$[OII]. In Fig. 9 we plot Hδ against $D_{n,4000}$. Local galaxies from the Sloan Digital Sky Survey are plotted for comparison.

The most striking trend is that group galaxies tend to show lower Hδ_F than cluster and field galaxies. This trend is particularly clear for blue galaxies, e.g., $D_{n,4000} < 1.4$. Blue galaxies in groups have smaller Hδ_F than blue galaxies in the field by ~3 Å. Local galaxies form a clear sequence, and field galaxies at $z = 1.2$ are on the same sequence with an extension to smaller $D_{n,4000}$. On the other hand, group galaxies occupy only the bottom half of the sequence, suggesting that they have systematically smaller Hδ_F. The cluster galaxies occupy the upper half, but, as noted above, one should be careful comparing these galaxies to the others because they are the brightest cluster members. The group and field galaxies are from the same observing run and the data reduction and spectral analysis were performed in exactly the same way. It seems inconceivable that the systematic offset in Hδ_F is due to observation biases. The trend seems to be real. Recall that Tanaka et al. (2007b) report that the faint end of the red sequence in these groups was truncated. Some of the group galaxies must be changing their properties, and the weak Hδ line provides us with a clue to identifying the main physical process behind the build-up of the red sequence.

In order to better understand the significance of the difference between field and group galaxies, we have added predictions from models to the plot. Bruzual & Charlot (2003) models are constructed with two star formation histories; a single burst model (denoted as SSP) and a τ model with $\tau = 1$ Gyr. We assume solar metallicity, a Salpeter initial mass function and no dust extinction (see Bruzual & Charlot 2003 for details). A sharp truncation of star formation makes Hδ very strong ~0.5 Gyr after the burst, while a gradual truncation does not trigger such an enhancement in Hδ (e.g., Couch & Sharples 1987; Poggianti et al. 1999). Very blue galaxies in the field have very strong Hδ absorptions, and they are consistent with an early phase of the single burst model. They may be undergoing intense starbursts. Such very blue galaxies are rare at $z = 0$ as seen from the distribution of the SDSS galaxies. The models do not reproduce the observed Hδ_F in group galaxies. Many group galaxies have weaker Hδ_F than the $\tau = 1$ Gyr model.

We further quantify star formation histories by measuring specific star formation rates (SSFR). The SSFR is defined as SSFR $=$ SFR$/M_*$ [yr^{-1}], where M_* is the stellar mass. Stellar masses are derived from the K band photometry taken with WFCAM (Tanaka et al. 2007b). We use Bruzual & Charlot (2003) models with different values for τ to estimate the stellar mass from the K band luminosity and the $i - K$ color. We assume solar-metallicity, a Salpeter initial mass function and no dust extinction. SFRs are estimated from the [OII] emission line (Kennicutt 1998). We apply a correction factor of ~30% for slit losses. We assume that all of our objects are point sources and estimate the slit losses from stars that were observed at the same time as the group and field galaxies.

We plot Hδ_F against SSFR in Fig. 10 along with two models representing different star formation timescales, a slowly decaying one with $\tau = 1$ Gyr and a rapidly decaying one with $\tau = 0.1$ Gyr. We cannot draw SSP model in the figure because SSFR goes to zero immediately after the burst. Instead we plot a $\tau = 0.1$ Gyr model to show the effect of different star formation time scales. Note that the SSFR shown in this figure is primarily sensitive to the current star formation activity, while $D_{n,4000}$ is sensitive to the integrated star formation history.

Galaxies with different star formation time scales occupy different parts of the plot. A short time scale model will enhance Hδ at early times, and the absorption remains relatively strong at

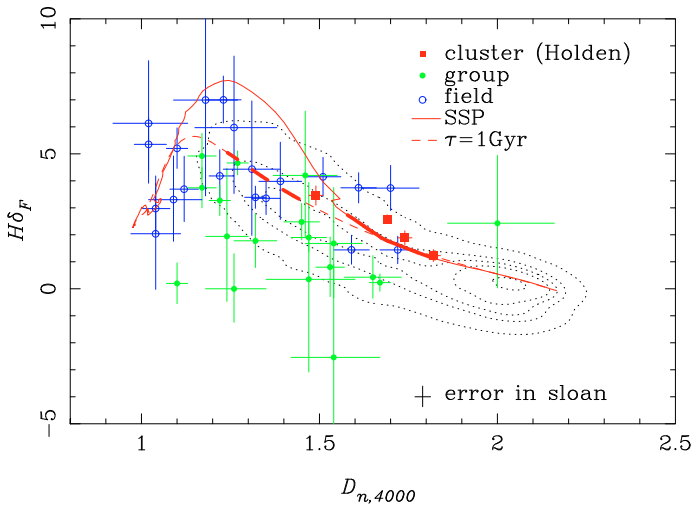

Fig. 9. Hδ_F plotted against $D_{n,4000}$ for galaxies in the cluster (red squares), the groups (filled circles) and the field (open circles). The contours show the distribution of galaxies from the SDSS for comparison. The contours enclose 5, 25, 50, 75 and 95 percent of the galaxy population. The typical error for the SDSS data is shown in the plot. The solid and dashed lines trace the path of the passively evolving and $\tau = 1$ Gyr models, respectively. The models start from the left (0 Gyr) and evolve to the right (13 Gyr). The thick part of the lines indicate the range of formation redshifts ($2 < z_f < 5$) for galaxies at $z = 1.2$.

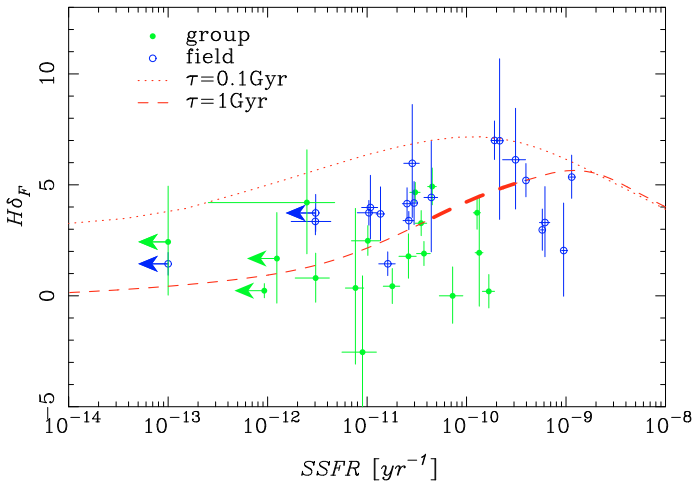

Fig. 10. Hδ_F plotted against specific SFR for galaxies in groups (filled circles) and the field (open circles). The dotted and dashed lines trace the path of the $\tau = 0.1$ and $\tau = 1$ Gyr models, respectively. The models start from the right and evolve to the left. The thick part of the lines indicate the range of formation redshifts $2 < z_f < 5$ for galaxies at $z = 1.2$. For $\tau = 0.1$ Gyr model, this redshift range is outside the plotted range.

small SSFRs. On the other hand, a long time scale model keeps Hδ weaker over almost all the plotted SSFR range. The position of a galaxy on the Hδ-$D_{n,4000}$ plot can be used to estimate the timescale on which galaxies stop forming stars based on the assumption of the exponentially decaying star formation rate.

The distribution of field galaxies in Fig. 10 (i.e., large SSFR) suggests that these galaxies have relatively short star formation time scales. They may be currently experiencing very active star formation. As seen in Fig. 9, a systematic offset in Hδ_F for galaxies in groups, in the sense that it is weaker in groups, is also seen in Fig. 10. The trend is not due to a strong mass dependency of galaxy properties (e.g., van der Wel et al. 2005). As a sanity

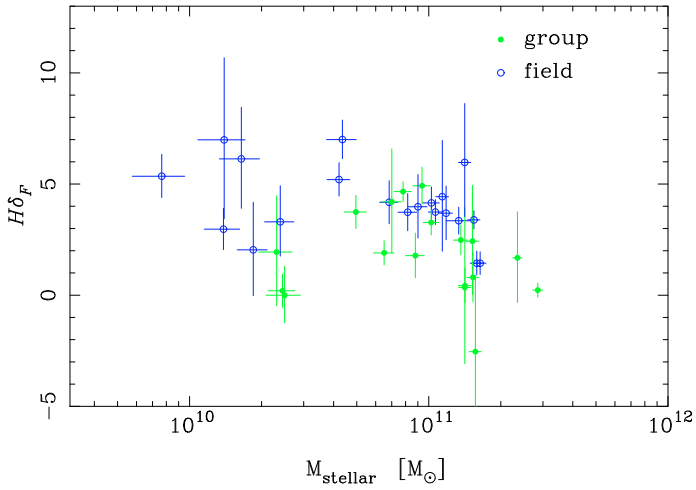

Fig. 11. Hδ_F plotted against stellar mass for galaxies in groups (filled circles) and field (open circles).

check, we plot Hδ_F against stellar mass in Fig. 11. Group galaxies have Hδ_F systematically weaker than field galaxies. Using galaxies with $>5 \times 10^{10}$ $M_\odot$, where we are reasonably complete, the median Hδ_F indices are 1.8 and 3.7 for group and field galaxies, respectively. The Kolmogorov-Smirnov test suggests that the two populations are drawn from the same parent population at <1% confidence level. The trend is therefore an environmental variation. We highlight again that the two samples are from the same observing run, and we reduced and analyzed them in exactly the same way. The difference is unlikely due to observation or selection biases.

The Hδ_F index can place constraints on the time scale on which galaxies quench their star formation activities as shown by the models in Figs. 9 and 10. There are several physical processes that could lead to the truncation of star formation. The time scale over which this occurs (the quenching time scale) is an important observational constraint, as it may help us understand the dominant process. In the next section, we will further discuss the trends we observe here and address implications of our results for galaxy evolution.

5. Discussions

We carried out the spectroscopic follow-up observations of the surrounding regions of the RDCSJ1252 cluster. We confirmed some of the photometrically identified structures and there seems to be at least two structures extending from the cluster. The large-scale structures at $z = 1.24$ give us a unique opportunity to look into star formation histories of galaxies as a function of environment. In this section, we extend discussions in the last section and address roles of environments on galaxy evolution.

Our primary findings in the previous section are summarized as follows.

1. There is a population of star-forming galaxies with red colors in groups and the field at $z \sim 1.2$. The core of RDCS1252 has very few galaxies of this type.
2. Galaxies in groups have systematically weaker Hδ lines than field galaxies.

A natural explanation for the first finding – the red colors of the star-forming galaxies – is that these galaxies are reddened by dust. Recent mid-infrared observations of clusters have shown that dusty star forming galaxies are found in the outskirts of

galaxy clusters. They tend to avoid the cluster core (e.g., Geach et al. 2006; Marcillac et al. 2007; Koyama et al. 2008). The same trend has been observed at $z \sim 0.2$ (Gallazzi et al. 2009; Wolf et al. 2009), although it does not necessarily hold in merging clusters (Haines et al. 2009)[1]. The red star forming galaxies that we find may be the optical counterparts of such galaxies. They are probably actively forming stars, as seen from the [OII] emission, but contain large amounts of dust, which reddens the rest frame optical colors.

The second finding – the relatively weak Hδ line in group galaxies – is unexpected. Star forming galaxies should have young stellar populations, and we expect to observe strong Hδ. The strength of the Hδ line in field galaxies is within expectations (the models can reproduce them as shown in the last section). The strength of the Hδ line in group galaxies is not.

The first point above may lead us to suggest that physical processes that triggers a sharp truncation is working in groups because starbursts can be induced by interactions, which can cause a sharp decline in star formation rates after the bursts. But, the second point may lead us to suggest the opposite because a gradual truncation is needed to suppress Hδ as shown in the last section. We argue in the following, however, that the second point could also suggest a sharp truncation scenario. To reach that point, we first have to explore dust extinction. It could be possible that a selective extinction of young stars in star forming regions absorb fluxes from early type stars and affect Hδ.

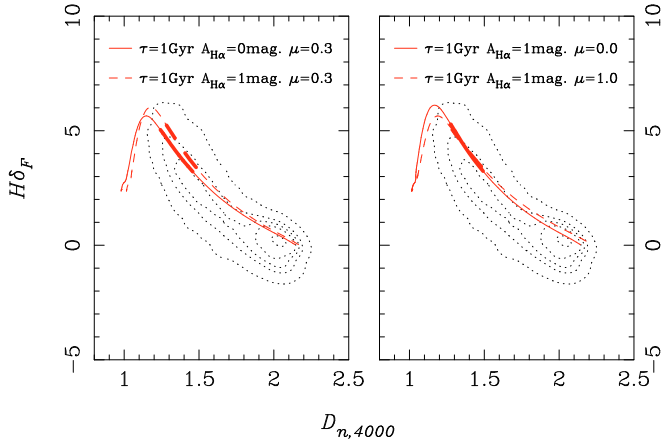

Fig. 12. Hδ plotted against $D_{n,4000}$. *Left panel*: the curves represent $\tau = 1$ Gyr star formation models with and without dust extinction. The fraction of ambient interstellar extinction is $\mu = 0.3$. The models start from the left (0 Gyr) and evolve to the right (13 Gyr). The thick part of the lines indicate the range of formation redshifts $2 < z_f < 5$ seen at $z = 1.2$. The contours show the distribution of galaxies from the Sloan survey for comparison. The contours enclose 5, 25, 50, 75 and 95 percent of the galaxies population. *Right panel*: $\tau = 1$ Gyr star formation models with an extinction of H$\alpha = 1$ mag. The solid and dashed curves are for models with $\mu = 0$ (i.e., extinction is entirely due to dust in star forming regions) and $\mu = 1$ (i.e., extinction is entirely due to ambient interstellar medium), respectively.

5.1. The effect of dust on the strength of Hδ

To quantify the effect of extinction on the Hδ and $D_{n,4000}$, we model two levels of extinction: no extinction, i.e., $A_{\mathrm{H}\alpha} = 0$ mag, and $A_{\mathrm{H}\alpha} = 1$ mag, which is typical for local star forming galaxies (Kennicutt 1998). Since we do not know the typical amount of extinction at this high redshift, we simply assume that it is the same as $z = 0$. To model the selective extinction of young stellar populations, we use the prescription described in Charlot & Fall (2000), which is incorporated in the Bruzual & Charlot (2003) models. Young stars ($<10^7$ yr) and older stars are affected by different amounts of dust and, the way dust affects Hδ and $D_{n,4000}$ is shown in Fig. 12.

$A_{\mathrm{H}\alpha} = 1$ mag of extinction makes $D_{n,4000}$ larger by ~0.1 at most. The $D_{n,4000}$ index is not strongly affected by dust because it is measured in a relatively narrow wavelength window. The Hδ_F index is larger by ~0.5 at its peak. For the fractional contribution of the ambient interstellar medium to the overall extinction, we used $\mu = 0.3$. This means, 70% of the extinction comes from star forming regions and it affects only newly born stars. The rest of the 30% comes from interstellar medium and it affects all stars. Young stars ($<10^7$ yr) born in star forming regions are therefore more obscured than A-type stars, resulting in larger values for Hδ_F at its peak. There is a large uncertainty in the time scale over which dust can obscure young stars, but it is very unlikely that the dust hides stars as long as 10^9 yr to completely obscure A-type stars (Blitz & Shu 1980).

We can also explore how varying selective extinction affects both Hδ_F and $D_{n,4000}$. The right panel in Fig. 12 shows models with $\mu = 0$ (i.e., the dust is confined to star forming regions) and $\mu = 1$ (i.e., the dust is distributed throughout the interstellar medium of the entire galaxy). Hδ_F is stronger at its peak in the $\mu = 0$ model for the same reason discussed above. $D_{n,4000}$ is larger by ~0.1 only at late times when old stars dominate the flux. While the effect of dust at $z = 1.2$ might be somewhat larger than we discuss here, it seems clear that dust alone is not able to change Hδ_F and $D_{n,4000}$ significantly. In particular, it cannot account for the weak Hδ_F observed in group galaxies. Dust can increase the Hδ absorption strengths, but cannot decrease them.

However, dust could affect the observed Hδ_F absorption in an indirect way. We used the [OII] flux to correct for Hδ emission from HII regions and to obtain the stellar Hδ absorption. Dust could affect this procedure, since the [OII] emission is prone to absorption by dust. The [OII] fluxes we actually observe are a lower limit of the unabsorbed [OII] fluxes. This will lead us to underestimate the Hδ emission, resulting in an underestimate to the stellar Hδ line strength. In converting from a [OII] flux to Hα flux and then to a Hδ flux we assumed $A_{\mathrm{H}\alpha} = 1$ mag. The weak Hδ_F index is particularly noticeable for blue ($D_{n,4000} \sim 1.2$) galaxies in groups. Hδ_F in these galaxies is ~3 Å smaller than Hδ_F in blue galaxies in the field.

If we assume that this difference is due to the star forming regions in group galaxies being dustier than the star forming regions in field galaxies, we find that $A_{\mathrm{H}\alpha} \sim 5$ mag of absorption in groups is needed to bring the strength of Hδ_F in these galaxies up to level observed in field galaxies. This is a significant amount of extinction, but it might not be too surprising given the result by Hicks et al. (2002), who obtained $E(B-V) \sim 1.1$ ($A_{\mathrm{H}\alpha} \sim 3$) from a handful of field galaxies at $0.8 < z < 1.6$. Such a significant amount of dust could strongly redden galaxies, but we do not observe galaxies redder than the red sequence (Fig. 8). Conroy et al. (2009) recently showed that colors of galaxies are much less affected by dust if the dust distribution is more clumpy. Their result suggests that it is not very straightforward to estimate dust contents of galaxies from broadband colors. Emission lines

[1] We note that Marcillac et al. (2008) showed that the distribution of stellar mass selected LIRGs and ULIRGs does not depend on environment. The difference might be due to large-scale structures. Marcillac et al. (2008) studied a blank field, while the other authors studied cluster fields, where structures are prominent. Isolated groups and those in rich structures might have different properties (see Croton et al. 2007 for a theoretical study of the assembly bias).

coming out of star forming regions may be a better tracer of dust, but our extinction from [OII] and Hδ will probably not be accurate enough to pin down the amount of dust in the groups.

We note that metallicity variations can also change Hδ_F, but the effect is relatively small. In Bruzual & Charlot (2003) models, super-solar ($Z = 0.05$) and subsolar ($Z = 0.008$) models result in differences of $|\Delta H\delta_F| \sim 0.3$ Å from the solar metallicity model. $D_{n,4000}$ is more strongly affected because it encompasses metal lines. Prochaska et al. (2007) showed that Hδ_F measurements are affected by the CN absorption on the redward side of Hδ. However, we observe a strong offset in Hδ_F not only in red galaxies, but also in blue galaxies for which we can safely ignore the effects of CN (Prochaska et al. 2007). Therefore, the observed Hδ_F offset is probably not due to metallicity variations.

As discussed above, strong dust extinction in the groups can bring the second point raised above into agreement with the first point. They both could point us to a physical process that truncates star formation on a short time scale. An interesting point here is that the galaxies are dustier in the groups, where the ongoing build-up of the red sequence is happening.

5.2. The physical process behind the build-up of the red sequence

The strong extinction may be an important clue to the driving process of the build-up of the red sequence. The driving physical process of the red sequence needs to be (1) effective in groups; (2) to trigger dusty starbursts; and (3) to suppresses star formation afterwards. Galaxy-galaxy interactions, for example, should occur most frequently in the group environment. These interactions can trigger dusty starbursts (e.g., Bridge et al. 2007). These large starbursts consume and expel a lot of the ingredients that are needed for future star formation episodes. At the end of the burst, there is little gas left for active star formation, which results in a sharp decline in star formation rates.

The observed weak Hδ absorptions may suggest that galaxy-galaxy interactions in groups are the driving physical process of the build-up of the red sequence and environment-dependent galaxy evolution. Galaxies exhaust their gas and stop their star formation in poor groups before they finally merge with the cluster core. This scenario is supported by other observations of lower redshift clusters (Tanaka et al. 2006, 2007a; Koyama et al. 2008). Elbaz et al. (2007) and Cooper et al. (2008) showed that the average SFR of galaxies increases with increasing galaxy density at $z \sim 1$. Although it is not straightforward to compare their results with ours, a part of the increase might be driven by the possible dusty starbursts in groups. One may wonder why we do not observe weak Hδ_F in the field. Starbursts may also happen in the field, but they may go unnoticed because they are masked by the active underlying star formation. It should be easier to detect them on top of relatively weak star formation. Interactions alone may not be able to reproduce the down-sizing phenomenon (Cowie et al. 1996), but massive galaxies may have experienced more mergers in the past than low-mass galaxies and they might have become red earlier.

While dust is one possible explanation, other explanations are possible. For example, a weak star burst on top of old stellar population might be able to reproduce the weak Hδ_F, although fine tuning of the relative fraction of the old and new stellar populations would be needed. We admit that it is not clear how to interpret Figs. 9 and 10, but it is clear that the *mode* of star formation is different in the group and field environments, as indicated by the systematic offset in Hδ. If it is because the star formation in group galaxies is highly obscured, then we would expect to see clear signatures of this in the near-infrared. For example, near infrared spectroscopy of the Hα and Hβ lines will tell us the amount of dust in star forming regions. High resolution imaging to obtain morphology of galaxies is another way to test this idea. If group galaxies are undergoing starbursts triggered by interactions, we should be able to see tidal features around some of the galaxies. In any case, it is clear that the *mode* of star formation at $z \sim 1.2$ depends on environment and that this may be an important clue to address the origin of the environment-dependent galaxy evolution.

6. Conclusions

We have carried out spectroscopic observations of the photometrically selected groups embedded in the large-scale structure surrounding the X-ray luminous galaxy cluster RDCS1252 at $z = 1.24$. Three groups contain galaxies at the cluster redshift. Two of them are embedded in a filamentary structure that extends northwards from the cluster core. The third group lies in a second structure that extends eastwards from the cluster. It is likely that all three groups are dynamically bound to the cluster. This is the first spectroscopic confirmation of large scale structure surrounding such a high redshift cluster.

We then quantified the spectral properties of galaxies at $z \sim 1.2$ in the cluster, group, and field with the $D_{n,4000}$, EW[OII], and Hδ_F indices. In both the field and the groups, we find that there is a significant population of [OII] emitting galaxies that are notable for their relatively red colors. The cluster core hosts few such galaxies. We also find that group galaxies have systematically weaker Hδ_F than field galaxies. We discussed the effects that dust can have on Hδ_F measurements and suggested that a possible way to interpret the weak Hδ_F is that the star forming regions in group galaxies are more dusty than those in field galaxies.

We then suggested that galaxy-galaxy interactions lead to a higher rate of dusty starbursts in group galaxies compared to the field. Interactions should occur more frequently between galaxies in groups than between field galaxies. Starbursts are effective at consuming and removing gas, which then leads to a sharp decrease in the star formation rate once the burst ends, thus leading to more red galaxies. We suggest that interactions are the driving physical process in the build-up of the red sequence and environment-dependent galaxy evolution. This scenario may not be the only way to interpret our results, but it is clear that the *mode* of star formation is dependent on environment at $z \sim 1.2$ as shown by the difference in Hδ_F between group and field galaxies. Near-infrared observations to measure Hα and high resolution imaging to obtain galaxy morphologies can be used to test this scenario.

Acknowledgements. This study is based on observations obtained at the European Southern Observatory using the ESO Very Large Telescope on Cerro Paranal through ESO program 081.A-0759. This study is also based on observations obtained at the Gemini Observatory through Subaru-Gemini time exchange program GS-2006B-Q14. The Gemini observatory is operated by the Association of Universities for Research in Astronomy, Inc., under a cooperative agreement with the NSF on behalf of the Gemini partnership: the National Science Foundation (United States), the Science and Technology Facilities Council (United Kingdom), the National Research Council (Canada), CONICYT (Chile), the Australian Research Council (Australia), Ministério da Ciência e Tecnologia (Brazil) and SECYT (Argentina). In addition, we used data collected at Subaru Telescope, which is operated by the National Astronomical Observatory of Japan, and data taken at the United Kingdom Infrared Telescope, which is operated by the Joint Astronomy Centre on behalf of the U.K. Particle Physics and Astronomy Research Council. The observations at the UKIRT 3.8-m telescope were supported by NAOJ. Funding for the SDSS and SDSS-II has

been provided by the Alfred P. Sloan Foundation, the Participating Institutions, the National Science Foundation, the U.S. Department of Energy, the National Aeronautics and Space Administration, the Japanese Monbukagakusho, the Max Planck Society, and the Higher Education Funding Council for England. The SDSS Web Site is http://www.sdss.org/. We thank Sune Toft for useful comments on the draft, and Arjen van der Wel and Brad Holden for kindly providing us with their spectra. We thank the anonymous referee for helpful comments, which improved the paper. This work was financially supported in part by the Grant-in-Aid for Scientific Research (Nos. 18684004 and 21340045) by the Japanese Ministry of Education, Culture, Sports and Science. AF has been partially supported trough NASA grant NNX08AD93G to UMBC.

References

Appenzeller, I., Fricke, K., Fürtig, W., et al. 1998, The Messenger, 94, 1
Balogh, M. L., Morris, S. L., Yee, H. K. C., Carlberg, R. G., & Ellingson, E. 1999, ApJ, 527, 54
Balogh, M., Eke, V., Miller, C., et al. 2004, MNRAS, 348, 1355
Beers, T. C., Geller, M. J., & Huchra, J. P. 1982, ApJ, 257, 23
Beers, T. C., Flynn, K., & Gebhardt, K. 1990, AJ, 100, 32
Bell, E. F., Wolf, C., Meisenheimer, K., et al. 2004, ApJ, 608, 752
Blakeslee, J. P., Franx, M., Postman, M., et al. 2003, ApJ, 596, L143
Blanton, M. R. 2006, ApJ, 648, 268
Blitz, L., & Shu, F. H. 1980, ApJ, 238, 148
Bridge, C. R., Appleton, P. N., Conselice, C. J., et al. 2007, ApJ, 659, 931
Bruzual, G., & Charlot, S. 2003, MNRAS, 344, 1000
Bundy, K., Ellis, R. S., Conselice, C. J., et al. 2006, ApJ, 651, 120
Cardelli, J. A., Clayton, G. C., & Mathis, J. S. 1989, ApJ, 345, 245
Carlberg, R. G., Yee, H. K. C., & Ellingson, E. 1997, ApJ, 478, 462
Charlot, S., & Fall, S. M. 2000, ApJ, 539, 718
Conroy, C., White, M., & Gunn, J. E. 2009, ArXiv e-prints
Cooper, M. C., Newman, J. A., Coil, A. L., et al. 2007, MNRAS, 376, 1445
Cooper, M. C., Newman, J. A., Weiner, B. J., et al. 2008, MNRAS, 383, 1058
Couch, W. J., & Sharples, R. M. 1987, MNRAS, 229, 423
Cowie, L. L., Songaila, A., Hu, E. M., & Cohen, J. G. 1996, AJ, 112, 839
Croton, D. J., Gao, L., & White, S. D. M. 2007, MNRAS, 374, 1303
Cucciati, O., Iovino, A., Marinoni, C., et al. 2006, A&A, 458, 39
Demarco, R., Rosati, P., Lidman, C., et al. 2005, A&A, 432, 381
Demarco, R., Rosati, P., Lidman, C., et al. 2007, ApJ, 663, 164
Dressler, A., Oemler, A. J., Couch, W. J., et al. 1997, ApJ, 490, 577
Elbaz, D., Daddi, E., Le Borgne, D., et al. 2007, A&A, 468, 33
Faber, S. M., Willmer, C. N. A., Wolf, C., et al. 2007, ApJ, 665, 265
Fisher, D., Fabricant, D., Franx, M., & van Dokkum, P. 1998, ApJ, 498, 195
Gallazzi, A., Bell, E. F., Wolf, C., et al. 2009, ApJ, 690, 1883
Geach, J. E., Smail, I., Ellis, R. S., et al. 2006, ApJ, 649, 661
Gobat, R., Rosati, P., Strazzullo, V., et al. 2008, A&A, 488, 853
Haines, C. P., Smith, G. P., Egami, E., et al. 2009, MNRAS, 396, 1297
Hicks, E. K. S., Malkan, M. A., Teplitz, H. I., McCarthy, P. J., & Yan, L. 2002, ApJ, 581, 205
Hilton, M., Stanford, S. A., Stott, J. P., et al. 2009, ArXiv e-prints
Holden, B. P., van der Wel, A., Franx, M., et al. 2005, ApJ, 620, L83
Hook, I. M., Jørgensen, I., Allington-Smith, J. R., et al. 2004, PASP, 116, 425
Hughes, J. P., Birkinshaw, M., & Huchra, J. P. 1995, ApJ, 448, L93
Kennicutt, Jr., R. C. 1998, ARA&A, 36, 189
Kodama, T., Smail, I., Nakata, F., Okamura, S., & Bower, R. G. 2001, ApJ, 562, L9
Kodama, T., Tanaka, M., Tamura, T., et al. 2005, PASJ, 57, 309
Koyama, Y., Kodama, T., Tanaka, M., Shimasaku, K., & Okamura, S. 2007, MNRAS, 382, 1719
Koyama, Y., Kodama, T., Shimasaku, K., et al. 2008, MNRAS, 391, 1758
Lidman, C., Rosati, P., Demarco, R., et al. 2004, A&A, 416, 829
Lidman, C., Rosati, P., Tanaka, M., et al. 2008, A&A, 489, 981
Lubin, L. M., Postman, M., & Oke, J. B. 1998, AJ, 116, 643
Marcillac, D., Rigby, J. R., Rieke, G. H., & Kelly, D. M. 2007, ApJ, 654, 825
Marcillac, D., Rieke, G. H., Papovich, C., et al. 2008, ApJ, 675, 1156
Mei, S., Holden, B. P., Blakeslee, J. P., et al. 2009, ApJ, 690, 42
Nakata, F., Kodama, T., Shimasaku, K., et al. 2005, MNRAS, 357, 1357
Poggianti, B. M., Smail, I., Dressler, A., et al. 1999, ApJ, 518, 576
Poggianti, B. M., Desai, V., Finn, R., et al. 2008, ApJ, 684, 888
Prochaska, L. C., Rose, J. A., Caldwell, N., et al. 2007, AJ, 134, 321
Rettura, A., Rosati, P., Nonino, M., et al. 2008, ArXiv e-prints
Rosati, P., Tozzi, P., Ettori, S., et al. 2004, AJ, 127, 230
Silverman, J. D., Kovač, K., Knobel, C., et al. 2009, ApJ, 695, 171
Stanford, S. A., Eisenhardt, P. R., Brodwin, M., et al. 2005, ApJ, 634, L129
Stanford, S. A., Romer, A. K., Sabirli, K., et al. 2006, ApJ, 646, L13
Strauss, M. A., Weinberg, D. H., Lupton, R. H., et al. 2002, AJ, 124, 1810
Strazzullo, V., Rosati, P., Stanford, S. A., et al. 2006, A&A, 450, 909
Tanaka, M., Kodama, T., Arimoto, N., et al. 2005, MNRAS, 362, 268
Tanaka, M., Kodama, T., Arimoto, N., & Tanaka, I. 2006, MNRAS, 365, 1392
Tanaka, M., Hoshi, T., Kodama, T., & Kashikawa, N. 2007a, MNRAS, 379, 1546
Tanaka, M., Kodama, T., Kajisawa, M., et al. 2007b, MNRAS, 377, 1206
Toft, S., Mainieri, V., Rosati, P., et al. 2004, A&A, 422, 29
van der Wel, A., Franx, M., van Dokkum, P. G., et al. 2005, ApJ, 631, 145
Wolf, C., Aragón-Salamanca, A., et al. 2009, MNRAS, 393, 1302
Worthey, G., & Ottaviani, D. L. 1997, ApJS, 111, 377
Yan, R., Newman, J. A., Faber, S. M., et al. 2006, ApJ, 648, 281
York, D. G., Adelman, J., Anderson, Jr., J. E., et al. 2000, AJ, 120, 1579

Table 2. The GMOS and FORS2 spectroscopic catalog, listing the object name (ID), the coordinates in J2000, the redshift, the confidence flag (0 for a secure redshift and 1 for a possible redshift), and the total magnitudes and their errors. The magnitudes are on the AB system. The redshift error does not include wavelength calibration error which is typically 0.2 Å. The magnitude of strongly blended objects is listed with a –1.

ID	RA	Dec.	Redshift	Flag	V	$\sigma(V)$	R	$\sigma(R)$	i	$\sigma(i)$	z	$\sigma(z)$	K	$\sigma(K)$
GMOS-F1-4	12 53 16.63	–29 17 11.6	$1.0706^{+0.0001}_{-0.0001}$	0	25.40	0.12	25.46	0.12	25.03	0.12	24.69	0.20	24.63	0.81
GMOS-F1-5	12 53 17.44	–29 17 00.8	$1.0684^{+0.0001}_{-0.0001}$	1	24.51	0.09	24.31	0.08	23.91	0.08	23.39	0.11	22.08	0.20
GMOS-F1-6	12 53 09.02	–29 16 47.6	$1.0976^{+0.0007}_{-0.0010}$	1	26.37	0.47	24.44	0.10	23.54	0.07	22.70	0.07	21.03	0.10
GMOS-F1-9	12 53 16.03	–29 16 17.2	$1.2452^{+0.0003}_{-0.0002}$	1	24.23	0.20	23.57	0.10	22.71	0.07	21.77	0.07	19.87	0.07
GMOS-F1-10	12 53 15.43	–29 16 23.7	$1.2354^{+0.0004}_{-0.0004}$	0	24.56	0.57	22.76	0.11	21.86	0.06	20.96	0.05	19.06	0.05
GMOS-F1-11	12 53 14.92	–29 16 13.4	$1.2368^{+0.0011}_{-0.0013}$	0	25.34	0.30	24.07	0.10	23.09	0.07	22.19	0.06	20.17	0.07
GMOS-F1-12	12 53 15.96	–29 16 29.9	$1.2839^{+0.0008}_{-0.0007}$	1	25.49	0.28	24.08	0.08	23.67	0.09	22.86	0.09	20.98	0.11
GMOS-F1-13	12 53 15.28	–29 16 29.8	$1.0699^{+0.0006}_{-0.0003}$	0	26.49	0.58	23.80	0.06	23.43	0.07	22.49	0.07	20.77	0.09
GMOS-F1-14	12 53 16.22	–29 16 38.4	$1.0698^{+0.0001}_{-0.0001}$	0	24.22	0.10	23.55	0.06	23.01	0.05	22.52	0.07	20.98	0.11
GMOS-F1-21	12 53 16.41	–29 15 44.0	$1.1797^{+0.0004}_{-0.0005}$	1	23.32	0.04	23.14	0.03	23.19	0.05	23.25	0.11	22.29	0.25
GMOS-F1-22	12 53 12.21	–29 16 04.5	$1.2360^{+0.0004}_{-0.0011}$	0	25.84	0.34	24.94	0.16	24.03	0.11	23.08	0.10	21.15	0.11
GMOS-F1-23	12 53 11.47	–29 16 06.4	$0.2504^{+0.0001}_{-0.0001}$	0	23.69	0.10	22.66	0.04	22.12	0.04	21.61	0.05	20.22	0.08
GMOS-F2-1	12 53 10.03	–29 19 34.8	$1.2313^{+0.0011}_{-0.0011}$	0	24.07	0.13	23.39	0.07	22.96	0.07	22.13	0.07	20.40	0.09
GMOS-F2-2	12 53 13.60	–29 19 40.1	$1.2354^{+0.0003}_{-0.0003}$	0	23.81	0.23	23.06	0.10	22.16	0.06	21.33	0.06	19.44	0.06
GMOS-F2-3	12 53 10.31	–29 19 37.5	$1.2350^{+0.0015}_{-0.0008}$	0	23.35	0.18	22.61	0.08	22.03	0.06	21.23	0.06	19.32	0.06
GMOS-F2-4	12 53 16.17	–29 19 27.8	$1.2367^{+0.0013}_{-0.0020}$	0	–1.00	–1.00	–1.00	–1.00	–1.00	–1.00	–1.00	–1.00	–1.00	–1.00
GMOS-F2-5	12 53 08.49	–29 19 58.2	$1.2262^{+0.0014}_{-0.0006}$	0	24.86	0.17	24.21	0.10	23.93	0.12	22.75	0.09	20.87	0.10
GMOS-F2-6	12 53 11.64	–29 19 54.5	$1.2327^{+0.0014}_{-0.0007}$	0	23.96	0.45	22.82	0.14	22.07	0.08	21.06	0.06	19.22	0.07
GMOS-F2-8	12 53 08.30	–29 20 10.5	$1.2341^{+0.0004}_{-0.0005}$	1	26.99	0.95	23.90	0.08	23.58	0.10	22.83	0.11	20.88	0.11
GMOS-F2-9	12 53 12.33	–29 19 47.3	$0.7294^{+0.0002}_{-0.0002}$	1	22.62	0.02	22.59	0.02	22.58	0.03	22.55	0.07	22.38	0.28
GMOS-F2-10	12 53 12.64	–29 20 00.1	$1.2335^{+0.0003}_{-0.0002}$	0	23.42	0.07	22.70	0.03	22.24	0.04	21.62	0.04	20.10	0.07
GMOS-F2-11	12 53 07.00	–29 20 05.4	$1.2312^{+0.0002}_{-0.0004}$	1	25.13	0.23	24.55	0.14	23.82	0.12	22.80	0.10	21.14	0.13
GMOS-F2-12	12 53 15.98	–29 20 26.5	$0.6696^{+0.0002}_{-0.0001}$	0	22.29	0.05	21.39	0.02	20.80	0.02	20.43	0.02	19.00	0.04
GMOS-F2-14	12 53 15.07	–29 20 22.3	$1.2977^{+0.0001}_{-0.0001}$	1	–1.00	–1.00	–1.00	–1.00	–1.00	–1.00	–1.00	–1.00	–1.00	–1.00
GMOS-F2-15	12 53 00.55	–29 21 34.4	$0.7427^{+0.0004}_{-0.0001}$	0	22.98	0.12	21.83	0.04	20.84	0.02	20.27	0.02	18.70	0.04
GMOS-F2-19	12 53 04.87	–29 22 09.9	$1.2160^{+0.0012}_{-0.0020}$	0	23.83	0.13	23.25	0.07	22.66	0.07	21.82	0.07	20.05	0.07
GMOS-F2-20	12 53 05.13	–29 22 20.4	$1.1764^{+0.0002}_{-0.0002}$	0	23.99	0.15	23.33	0.08	22.57	0.06	21.64	0.06	19.86	0.06
GMOS-F2-21	12 53 06.67	–29 22 16.8	$1.2370^{+0.0008}_{-0.0004}$	1	24.53	0.14	24.36	0.12	23.43	0.09	22.59	0.09	20.82	0.10
GMOS-F3-1	12 53 52.55	–29 25 57.5	$1.0997^{+0.0010}_{-0.0007}$	0	23.93	0.20	23.06	0.08	22.45	0.07	21.46	0.06	19.83	0.07
GMOS-F3-2	12 53 49.70	–29 24 35.5	$1.2336^{+0.0001}_{-0.0001}$	0	24.25	0.17	23.74	0.10	23.16	0.10	22.25	0.09	20.64	0.11
GMOS-F3-4	12 53 47.32	–29 23 28.4	$1.0979^{+0.0003}_{-0.0002}$	0	23.99	0.09	23.90	0.08	23.05	0.06	22.18	0.06	20.49	0.08
GMOS-F3-6	12 53 46.75	–29 22 52.4	$1.0957^{+0.0001}_{-0.0001}$	1	24.03	0.08	23.82	0.07	23.47	0.07	23.36	0.14	23.05	0.49
GMOS-F3-7	12 53 49.75	–29 24 27.3	$0.7497^{+0.0001}_{-0.0001}$	0	24.80	0.14	23.66	0.05	22.70	0.03	22.22	0.05	21.19	0.12
GMOS-F3-8	12 53 52.15	–29 25 03.0	$0.7620^{+0.0003}_{-0.0016}$	0	24.48	0.17	23.18	0.05	22.48	0.05	22.00	0.06	21.13	0.14
GMOS-F3-9	12 53 46.60	–29 23 05.9	$0.9355^{+0.0002}_{-0.0001}$	1	24.36	0.14	23.55	0.07	22.64	0.05	21.91	0.05	20.41	0.08
GMOS-F3-10	12 53 45.09	–29 25 04.7	$1.1529^{+0.0002}_{-0.0001}$	1	25.80	0.49	23.45	0.07	22.67	0.05	21.74	0.05	20.03	0.06
GMOS-F3-13	12 53 42.79	–29 24 42.6	$1.2511^{+0.0010}_{-0.0011}$	1	24.84	0.25	23.61	0.08	22.67	0.06	21.77	0.05	19.68	0.05
GMOS-F3-14	12 53 42.91	–29 25 20.3	$1.1782^{+0.0002}_{-0.0003}$	0	25.84	0.32	24.54	0.11	23.69	0.08	22.81	0.08	21.19	0.11
GMOS-F3-16	12 53 43.92	–29 25 56.9	$1.1725^{+0.0010}_{-0.0006}$	0	23.15	1.32	22.23	0.60	21.87	0.23	21.26	0.19	20.04	0.89
GMOS-F3-17a	12 53 44.01	–29 25 16.8	$1.1726^{+0.0005}_{-0.0009}$	1	24.27	0.25	23.12	0.08	22.50	0.07	21.56	0.06	19.89	0.07
GMOS-F3-17b	12 53 43.72	–29 25 19.2	$1.1773^{+0.0003}_{-0.0001}$	1	25.30	0.25	23.90	0.08	23.01	0.05	22.04	0.05	20.22	0.07
GMOS-F3-18	12 53 43.39	–29 25 38.9	$1.1673^{+0.0009}_{-0.0007}$	0	24.19	0.11	23.70	0.07	23.17	0.07	22.37	0.07	20.44	0.08
GMOS-F3-20	12 53 39.98	–29 26 20.6	$0.9335^{+0.0001}_{-0.0001}$	0	24.19	0.10	23.45	0.05	22.69	0.04	22.01	0.05	20.50	0.08
GMOS-F3-22	12 53 36.43	–29 25 09.5	$0.7516^{+0.0003}_{-0.0003}$	0	24.59	0.13	23.68	0.06	23.11	0.05	22.56	0.07	20.84	0.09
GMOS-F3-23	12 53 38.47	–29 26 22.9	$0.4659^{+0.0001}_{-0.0001}$	0	23.83	0.05	23.52	0.04	23.31	0.04	23.56	0.12	23.87	0.66
GMOS-F3-26	12 53 36.07	–29 26 01.8	$0.5423^{+0.0001}_{-0.0001}$	0	23.84	0.06	23.27	0.04	23.21	0.05	23.23	0.11	23.02	0.43
FORS2-F1-1	12 53 13.22	–29 19 11.3	$1.2314^{+0.0001}_{-0.0001}$	0	22.82	0.05	22.56	0.04	22.35	0.05	21.68	0.05	20.47	0.10
FORS2-F1-2	12 53 07.72	–29 19 17.7	$1.2120^{+0.0004}_{-0.0004}$	0	23.26	0.31	22.55	0.13	22.06	0.08	21.29	0.07	19.82	0.13
FORS2-F1-3	12 53 05.85	–29 19 55.3	$1.2127^{+0.0008}_{-0.0009}$	0	25.24	0.33	23.88	0.10	23.06	0.08	22.01	0.07	20.24	0.07
FORS2-F1-4	12 52 58.94	–29 19 15.2	$1.0982^{+0.0002}_{-0.0001}$	0	23.42	0.12	22.76	0.06	22.29	0.06	21.52	0.06	20.26	0.09
FORS2-F1-5	12 53 03.07	–29 19 59.2	$1.0893^{+0.0002}_{-0.0002}$	0	24.16	0.09	23.72	0.06	23.23	0.06	22.62	0.07	21.30	0.13

Table 2. continued.

ID	RA	Dec.	Redshift	Flag	V	$\sigma(V)$	R	$\sigma(R)$	i	$\sigma(i)$	z	$\sigma(z)$	K	$\sigma(K)$
FORS2-F1-6	12 53 04.58	–29 20 38.7	$1.3200^{+0.0005}_{-0.0004}$	0	24.08	0.09	23.38	0.04	23.12	0.06	22.20	0.05	20.60	0.08
FORS2-F1-7	12 53 03.60	–29 21 26.2	$1.1856^{+0.0007}_{-0.0005}$	0	24.15	0.08	23.59	0.05	23.19	0.06	22.40	0.06	20.93	0.10
FORS2-F1-8	12 53 00.79	–29 17 57.1	$1.0868^{+0.0002}_{-0.0001}$	0	23.96	0.08	23.50	0.06	23.00	0.06	22.37	0.07	21.04	0.12
FORS2-F1-9	12 53 10.94	–29 21 43.7	$1.2135^{+0.0009}_{-0.0004}$	0	26.07	0.46	24.42	0.12	23.40	0.08	22.33	0.06	20.22	0.07
FORS2-F1-10	12 53 11.08	–29 22 40.5	$1.1876^{+0.0002}_{-0.0002}$	0	23.83	0.07	23.42	0.05	22.98	0.06	22.18	0.06	20.32	0.07
FORS2-F1-11	12 53 06.67	–29 22 16.8	$1.2164^{+0.0006}_{-0.0007}$	0	24.53	0.14	24.36	0.12	23.43	0.09	22.59	0.09	20.82	0.10
FORS2-F1-12	12 53 08.11	–29 21 43.1	$1.2390^{+0.0002}_{-0.0003}$	0	24.18	0.09	23.73	0.06	23.29	0.06	22.53	0.07	21.08	0.11
FORS2-F1-13	12 52 58.36	–29 18 45.6	$1.1491^{+0.0001}_{-0.0001}$	0	23.78	0.06	23.45	0.05	23.08	0.05	22.50	0.07	21.45	0.15
FORS2-F1-14	12 53 11.99	–29 20 17.6	$1.0541^{+0.0013}_{-0.0016}$	0	24.72	0.13	24.12	0.08	23.68	0.08	22.99	0.09	21.37	0.13
FORS2-F1-15	12 53 06.04	–29 19 15.2	$1.2398^{+0.0007}_{-0.0006}$	0	24.25	0.11	24.15	0.10	23.79	0.12	22.70	0.09	21.69	0.19
FORS2-F1-16	12 53 09.83	–29 18 56.4	$1.3204^{+0.0003}_{-0.0003}$	0	24.99	0.22	24.19	0.11	23.70	0.11	22.75	0.10	20.98	0.12
FORS2-F1-17	12 53 08.71	–29 18 25.0	$0.3070^{+0.0001}_{-0.0001}$	0	21.42	0.02	21.06	0.01	21.01	0.02	20.70	0.03	20.10	0.08
FORS2-F1-18	12 53 11.25	–29 19 29.8	$0.6203^{+0.0002}_{-0.0001}$	0	23.03	0.04	22.44	0.02	22.28	0.03	22.43	0.07	22.59	0.36
FORS2-F1-19	12 53 11.52	–29 15 09.4	$1.2367^{+0.0007}_{-0.0011}$	0	25.12	0.23	24.26	0.11	23.38	0.08	22.37	0.07	20.26	0.07
FORS2-F1-20	12 53 15.43	–29 16 23.7	$1.2364^{+0.0006}_{-0.0006}$	0	24.56	0.57	22.76	0.11	21.86	0.06	20.96	0.05	19.06	0.05
FORS2-F1-21	12 53 16.87	–29 16 17.9	$0.8856^{+0.0001}_{-0.0002}$	0	24.22	0.13	23.28	0.06	22.65	0.05	22.11	0.07	20.23	0.07
FORS2-F1-22	12 53 17.75	–29 17 29.0	$1.2320^{+0.0002}_{-0.0001}$	0	23.13	0.12	22.84	0.08	22.48	0.08	21.82	0.08	20.84	0.17
FORS2-F1-23	12 53 08.35	–29 16 01.8	$1.2113^{+0.0001}_{-0.0001}$	0	24.67	0.19	23.72	0.08	23.13	0.08	22.38	0.08	20.54	0.09
FORS2-F1-25	12 53 19.08	–29 18 12.0	$1.0680^{+0.0003}_{-0.0005}$	0	23.55	0.09	23.45	0.08	23.07	0.09	22.35	0.10	21.62	0.23
FORS2-F1-26	12 53 04.36	–29 17 16.8	$1.1020^{+0.0001}_{-0.0001}$	0	21.97	0.02	21.75	0.01	21.41	0.02	20.98	0.02	20.00	0.06
FORS2-F1-27	12 53 03.67	–29 16 02.1	$1.0858^{+0.0002}_{-0.0002}$	0	24.38	0.11	23.66	0.06	23.08	0.05	22.31	0.06	20.85	0.10
FORS2-F1-28	12 53 24.74	–29 16 59.8	$1.1415^{+0.0001}_{-0.0002}$	0	23.70	0.09	23.50	0.07	23.33	0.10	22.80	0.13	21.93	0.27
FORS2-F1-29	12 53 11.49	–29 18 25.7	$1.1976^{+0.0001}_{-0.0001}$	0	23.31	0.05	23.06	0.04	22.76	0.04	22.22	0.06	21.13	0.12
FORS2-F1-30	12 53 15.96	–29 17 58.8	$0.5750^{+0.0001}_{-0.0002}$	0	21.74	0.06	21.12	0.03	20.93	0.03	20.83	0.04	20.31	0.15
FORS2-F1-31	12 53 17.95	–29 18 44.2	$0.0000^{+0.0001}_{-0.0001}$	0	23.39	0.06	22.50	0.03	21.58	0.02	21.03	0.02	20.46	0.08
FORS2-F2-1	12 53 45.09	–29 25 04.7	$1.1736^{+0.0009}_{-0.0010}$	0	25.80	0.49	23.45	0.07	22.67	0.05	21.74	0.05	20.03	0.06
FORS2-F2-2	12 53 42.09	–29 23 31.2	$1.3044^{+0.0001}_{-0.0001}$	0	22.74	0.04	22.42	0.03	22.11	0.03	21.53	0.04	20.37	0.08
FORS2-F2-3	12 53 50.15	–29 24 02.8	$1.2318^{+0.0002}_{-0.0002}$	0	23.31	0.10	22.94	0.06	22.48	0.07	21.83	0.07	20.32	0.09
FORS2-F2-4	12 53 49.63	–29 24 39.3	$1.2355^{+0.0002}_{-0.0002}$	0	23.68	0.10	23.01	0.05	22.56	0.06	21.77	0.06	20.34	0.08
FORS2-F2-5	12 53 44.52	–29 23 21.8	$1.1724^{+0.0001}_{-0.0001}$	0	23.01	0.06	23.03	0.06	22.71	0.07	22.14	0.08	21.38	0.19
FORS2-F2-6	12 53 57.09	–29 25 41.0	$1.0938^{+0.0004}_{-0.0008}$	0	23.27	0.07	22.88	0.05	22.49	0.05	21.84	0.06	20.53	0.10
FORS2-F2-7	12 53 56.85	–29 24 52.7	$1.2348^{+0.0001}_{-0.0002}$	0	25.30	0.31	24.33	0.14	23.28	0.09	22.14	0.07	20.39	0.08
FORS2-F2-8	12 53 57.91	–29 24 50.0	$1.2377^{+0.0001}_{-0.0002}$	0	23.97	0.08	23.48	0.05	23.04	0.05	22.42	0.07	21.15	0.12
FORS2-F2-9	12 53 59.08	–29 24 39.8	$1.2355^{+0.0003}_{-0.0002}$	0	23.98	0.15	23.41	0.09	22.87	0.08	22.13	0.09	20.50	0.10
FORS2-F2-10	12 54 01.00	–29 25 01.8	$1.2366^{+0.0006}_{-0.0011}$	0	24.68	0.20	23.85	0.09	23.06	0.07	22.16	0.07	20.19	0.07
FORS2-F2-11	12 53 42.47	–29 25 18.8	$1.1791^{+0.0008}_{-0.0015}$	0	25.30	0.22	24.70	0.13	23.97	0.11	22.81	0.08	21.09	0.11
FORS2-F2-12	12 53 57.23	–29 24 20.2	$1.1600^{+0.0004}_{-0.0008}$	0	24.70	0.24	23.90	0.12	23.40	0.12	22.22	0.09	20.60	0.10
FORS2-F2-13	12 53 42.02	–29 24 14.4	$1.3998^{+0.0014}_{-0.0009}$	1	27.11	0.81	24.81	0.14	23.90	0.09	22.92	0.08	20.85	0.09
FORS2-F2-14a	12 53 43.72	–29 25 19.2	$1.1784^{+0.0004}_{-0.0005}$	0	25.30	0.25	23.90	0.08	23.01	0.05	22.04	0.05	20.22	0.07
FORS2-F2-14b	12 53 43.87	–29 25 17.7	$1.1696^{+0.0018}_{-0.0019}$	1	23.87	0.35	22.82	0.12	22.08	0.07	21.11	0.05	19.35	0.07
FORS2-F2-14c	12 53 44.01	–29 25 16.8	$1.1749^{+0.0007}_{-0.0008}$	0	24.27	0.25	23.12	0.08	22.50	0.07	21.56	0.06	19.89	0.07
FORS2-F2-15	12 53 54.76	–29 24 31.4	$1.2340^{+0.0002}_{-0.0001}$	0	23.01	0.07	22.30	0.03	21.99	0.04	21.63	0.06	20.94	0.15
FORS2-F2-16	12 53 54.71	–29 25 07.9	$0.9668^{+0.0001}_{-0.0001}$	0	22.84	0.03	22.70	0.03	22.23	0.03	22.06	0.05	22.04	0.23
FORS2-F2-18	12 53 46.60	–29 23 05.9	$0.9364^{+0.0001}_{-0.0001}$	0	24.36	0.14	23.55	0.07	22.64	0.05	21.91	0.05	20.41	0.08
FORS2-F2-19	12 53 44.78	–29 23 08.3	$0.5618^{+0.0002}_{-0.0001}$	0	22.29	0.02	21.80	0.01	21.59	0.02	21.57	0.04	21.27	0.15
FORS2-F2-21	12 53 39.07	–29 25 38.5	$1.0948^{+0.0001}_{-0.0002}$	0	23.55	0.07	23.01	0.04	22.55	0.04	21.86	0.05	20.60	0.09
FORS2-F2-22a	12 53 39.59	–29 25 26.7	$1.3016^{+0.0008}_{-0.0009}$	0	25.19	0.28	23.95	0.10	23.00	0.07	22.01	0.06	20.03	0.06
FORS2-F2-22b	12 53 39.48	–29 25 27.6	$0.0000^{+0.0001}_{-0.0001}$	0	25.31	0.20	24.26	0.08	23.14	0.05	22.45	0.06	21.49	0.14
FORS2-F2-23	12 53 37.96	–29 27 32.8	$1.2366^{+0.0004}_{-0.0004}$	0	22.91	0.05	22.52	0.04	22.17	0.04	21.41	0.04	19.96	0.07
FORS2-F2-24	12 53 31.63	–29 26 08.1	$1.3287^{+0.0001}_{-0.0001}$	0	22.96	0.05	22.80	0.04	22.71	0.06	22.19	0.08	21.35	0.18
FORS2-F2-25	12 53 27.93	–29 25 15.2	$1.2326^{+0.0001}_{-0.0001}$	0	23.51	0.05	23.30	0.04	23.05	0.05	22.43	0.06	21.87	0.20
FORS2-F2-26	12 53 44.37	–29 26 55.8	$1.3205^{+0.0002}_{-0.0001}$	0	23.68	0.07	23.52	0.06	23.44	0.09	22.91	0.11	22.00	0.25

Table 2. continued.

ID	RA	Dec.	Redshift	Flag	V	$\sigma(V)$	R	$\sigma(R)$	i	$\sigma(i)$	z	$\sigma(z)$	K	$\sigma(K)$
FORS2-F2-27	12 53 33.40	–29 23 57.6	$1.1713^{+0.0001}_{-0.0001}$	0	24.71	0.13	24.36	0.09	24.00	0.10	22.98	0.09	22.38	0.28
FORS2-F2-28	12 53 38.03	–29 26 31.1	$1.3047^{+0.0004}_{-0.0005}$	0	24.61	0.16	23.68	0.07	22.93	0.06	21.95	0.05	20.40	0.08
FORS2-F2-29	12 53 31.27	–29 26 51.1	$1.2294^{+0.0001}_{-0.0001}$	0	23.28	0.05	23.13	0.04	23.05	0.06	22.57	0.09	22.27	0.31
FORS2-F2-30	12 53 32.25	–29 26 05.3	$1.3264^{+0.0002}_{-0.0002}$	0	25.24	0.22	24.16	0.09	23.67	0.09	22.90	0.09	20.96	0.10
FORS2-F2-33	12 53 30.14	–29 24 52.8	$0.3833^{+0.0001}_{-0.0001}$	0	23.09	0.04	22.71	0.03	22.69	0.04	22.52	0.07	22.74	0.40
FORS2-F3-1	12 52 12.16	–29 31 11.8	$1.1742^{+0.0005}_{-0.0004}$	0	24.63	0.21	23.31	0.07	22.43	0.05	21.36	0.04	19.59	0.05
FORS2-F3-3	12 52 09.98	–29 31 23.9	$1.1748^{+0.0004}_{-0.0003}$	0	24.43	0.16	23.57	0.07	22.85	0.06	21.84	0.05	20.08	0.07
FORS2-F3-5	12 52 04.99	–29 29 20.1	$1.1919^{+0.0004}_{-0.0003}$	0	23.77	0.10	23.07	0.05	22.55	0.05	21.70	0.05	19.99	0.07
FORS2-F3-6	12 52 07.12	–29 31 29.6	$1.1233^{+0.0009}_{-0.0010}$	0	23.31	0.19	22.59	0.09	21.91	0.06	21.17	0.06	19.24	0.06
FORS2-F3-7	12 52 06.19	–29 30 23.9	$1.3293^{+0.0002}_{-0.0001}$	0	23.56	0.07	23.12	0.04	22.97	0.06	22.27	0.07	21.48	0.17
FORS2-F3-8	12 52 03.00	–29 33 19.1	$1.1973^{+0.0001}_{-0.0001}$	0	23.26	0.04	22.98	0.03	22.72	0.04	22.24	0.05	21.65	0.17
FORS2-F3-10	12 52 03.98	–29 32 49.1	$1.0819^{+0.0003}_{-0.0003}$	1	24.18	0.12	23.91	0.09	23.44	0.10	22.68	0.10	22.21	0.31
FORS2-F3-13	12 52 13.48	–29 31 26.6	$1.3380^{+0.0005}_{-0.0002}$	1	23.39	0.05	23.04	0.03	22.92	0.05	22.28	0.06	21.18	0.12
FORS2-F3-14	12 52 14.56	–29 33 08.8	$0.9106^{+0.0001}_{-0.0002}$	0	24.33	0.10	23.86	0.06	23.64	0.08	22.74	0.08	22.18	0.24
FORS2-F3-16	12 52 01.55	–29 31 26.5	$0.2951^{+0.0001}_{-0.0001}$	0	24.37	0.06	24.06	0.05	24.03	0.06	23.87	0.12	23.49	0.44
FORS2-F3-18	12 52 19.70	–29 30 34.4	$1.2463^{+0.0005}_{-0.0007}$	1	23.28	0.16	22.54	0.07	22.08	0.06	21.47	0.07	19.80	0.08
FORS2-F3-19	12 52 25.41	–29 29 22.5	$1.2443^{+0.0002}_{-0.0001}$	0	22.85	0.05	22.59	0.04	22.29	0.04	21.77	0.06	21.23	0.16
FORS2-F3-20	12 52 28.68	–29 31 46.9	$1.1505^{+0.0004}_{-0.0004}$	0	23.47	0.06	23.02	0.04	22.51	0.04	21.77	0.04	20.26	0.07
FORS2-F3-23	12 52 18.33	–29 33 24.5	$1.2922^{+0.0004}_{-0.0005}$	0	24.46	0.16	24.02	0.11	23.29	0.09	22.29	0.08	20.44	0.08
FORS2-F3-24	12 52 27.21	–29 33 13.7	$1.2348^{+0.0002}_{-0.0002}$	0	23.35	0.06	23.06	0.04	22.84	0.06	22.27	0.07	21.80	0.23
FORS2-F3-25	12 52 20.61	–29 33 23.2	$1.3015^{+0.0002}_{-0.0003}$	0	23.22	0.06	22.88	0.04	22.70	0.06	22.07	0.07	20.91	0.13
FORS2-F3-26	12 52 21.62	–29 33 26.4	$1.2165^{+0.0004}_{-0.0004}$	1	24.81	0.16	24.11	0.09	23.85	0.11	22.98	0.11	21.56	0.16
FORS2-F3-29	12 52 29.25	–29 31 19.8	$1.1061^{+0.0012}_{-0.0028}$	1	26.39	0.65	23.97	0.09	23.16	0.07	22.10	0.06	20.28	0.07